Silicon Photomultipliers as Free Space Optical Communication Sensors

by

Leonardo Gallo de la Paz

B.S. Aeronautical Engineering, Rensselaer Polytechnic Institute (2020)

Submitted to the Department of Aeronautics and Astronautics
in partial fulfillment of the requirements for the degree of

Master of Science in Aeronautics and Astronautics

at the

MASSACHUSETTS INSTITUTE OF TECHNOLOGY

May 2024

Authored by: ____________________

Leonardo Gallo de la Paz
Department of Aeronautics and Astronautics
May 17, 2024

Certified by ____________________

Kerri L. Cahoy
Sheila Evans Widnall Professor of Aeronautics and Astronautics
Bisplinghoff Faculty Fellow
Thesis Supervisor

Accepted by ____________________

Jonathan P. How
R. C. Maclaurin Profesor of Aeronautics and Astronautics
Chair, Graduate Program Committee

Silicon Photomultipliers as Free Space Optical Communication Sensors

by

Leonardo Gallo de la Paz

Submitted to the Department of Aeronautics and Astronautics
on May 17, 2024, in partial fulfillment of the
requirements for the degree of
Master of Science in Aeronautics and Astronautics

Abstract

Free-space optical communications (FSOC) is a growing field that presents an attractive alternative to the the current technology standard of radio frequency (RF) communications. Typical optical carriers have smaller SWaP in comparison to RF systems due to the difference in required aperture sizes. The narrower beam divergence of optical wavelengths also results in a higher power efficiency for long range communication links. This improvement in performance can be leveraged by platforms constrained by size, such as satellites. For the past ten years, the number of satellites launched has increased by an order of magnitude, with smallsats currently making up 96% of the launched vehicles. The use of FSOC terminals for smallsats enables higher data rates but requires precise pointing. An example nanosatellite FSOC mission, NASA's CubeSat Laser Infrared CrosslinK (CLICK) B/C addresses this by using a beacon-based pointing, acquisition, and tracking (PAT) system to correct for angular misalignment while an avalanche photodiode (APD) receiver detects the communication signal. The high gain of the APD allows the communication signal to be detected at link distances ranging from 25 km to 580 km for CLICK-B/C. In this work, we consider whether higher sensitivities may be achieved by using a Silicon photomultiplier (SiPM) as a receive optical sensor. SiPMs are arrays of APDs operated in Geiger mode, characterized by nanosecond output pulses and gains in the order of 10^6 electrons per photon. This thesis proposes using a SiPM in a 2x2 pixel configuration as a dual pointing and communication sensor for FSOC terminals in LEO. In this configuration the misalignment of the optical signal between the transmit and receive terminals can be directly measured by the SiPM, eliminating the need for a dedicated beacon laser and quadcell detector used for PAT. This reduces the overall SWaP of the communication terminal by a factor of 2. The pointing performance of the proposed SiPM configuration is characterized by calculating the noise equivalent angle (NEA) of the detector through simulation and experiment, and the communication performance is evaluated by testing the maximum detectable pulsing frequency of a laser. The simulation results support an NEA of 1 µrad and a maximum detectable pulsing rate of 2 GHz.

Thesis Supervisor: Kerri L. Cahoy

Title: Sheila Evans Widnall Professor of Aeronautics and Astronautics, Bisplinghoff Faculty Fellow

Acknowledgements

For the past two years I've had the privilege of living in a community rich beyond belief. The enabling environment at MIT has allowed me to conceive and implement ideas that I would have never thought possible. Reaching such a place was made possible by caring people who I'd like to dedicate this thesis to.

I thank my family for their loving support and encouragement throughout my life. They have continuously given me the courage necessary to follow my dreams in uncharted territory. Los quiero con toda el alma.

I'd also like to thank my advisor, Professor Kerri Cahoy, for giving me a space in STAR Lab to pursue my research interests alongside bright and caring people. Special thanks to the members of the CLICK-B/C team for their continued guidance and excellent technical advice. Being a member of STAR Lab has allowed me to work on incredible projects with paramount freedom.

This research is funded by the Draper Scholars program. I'd like to thank Dr. J.P. Laine for his contagious excitement and strong belief in young generations. From my first internship at Draper in 2017 to my acceptance into the Draper Scholars program, J.P. has never failed to ask me about exciting ideas and coming up with plans to implement them. I'd also like to thank my Draper advisor, Dr. Joseph Hollmann, for his mentorship and continued support during the prototyping phases of this project. His creative ideas and practical implementations have shown me what it looks like to be an inventor. Additionally, a thank you to Group Leader Carl Hansen for sharing his edge sensor modeling with me. The SiPM simulation presented on this thesis would not be possible without him.

Last but not least, I'd like to thank Marta for all her help throughout my time at MIT. From reading each carefully worded sentence in my application to throwing study breaks as Baker GRA's, it has been truly memorable to share this experience with you.

Contents

List of Figures

List of Tables

Chapter 1

Introduction

1.1 Motivation

The transmission of data through free-space has been dominated by radio frequency technologies for more than 100 years, starting with the public broadcast of the Harding-Cox presidential election by the Westinghouse Electric and Manufacturing Company in Pittsburgh on November 22, 1920 [1]. From that day on, radio frequencies have been used to broadcast audio, video, and timing information to the general public. The technology is now being augmented by systems pushing to use shorter wavelengths in the electromagnetic spectrum, which can have advantages in size and efficiency for applications where the higher loss and increased pointing can be supported.

Free-space optical communications (FSCOC), or lasercom, makes use of wavelengths in the visible and near IR range of the electromagnetic spectrum to transmit data. The shorter optical wavelengths in the visible and infrared spectrum have reduced diffraction losses due to narrower beamwidths. This enables smaller aperture sizes for optical systems, reducing the overall size weight and power (SWAP) of the communications terminal. A narrow beamwidth also increases the security in a communication link by making it harder to intercept the signal. The point to point nature of optical links offers secure connections for a currently unregulated part of the spectrum. The optical spectrum offers large amounts of bandwidth for lasercom systems, although physics plays a role in that there are certain preferred wavelengths where laser sources are more efficient, such as 1064 nm and 1550 nm.

Free space optical path losses, atmospheric disturbances, and optical alignment of the transceiver terminals as well as internal alignment and packaging are the main challenges in FSOC. For a space to space satellite crosslink connection, the satellite terminals must have adequate pointing, acquisition, and tracking (PAT) control to transmit and receive signals. Additionally, the detector at the receiver must be sensitive enough to detect the signal. The development of compact lasercom systems with adequate PAT control and low power detection can transform small satellites into cost effective science and technology platforms with high data throughput.

Figure 1-1 summarizes the increase in small satellite launches for the last 10 years. The number of small satellites launched has increased by more than an order of magnitude. Communication satellites such as the Starlink and OneWeb constellations make up more than 75% of all smallsats launched in 2022. The increase in communication launches highlights the push in industry to provide higher crosslink and downlink data rates to avoid "bottlenecks" of data in space. These satellites will encounter pointing challenges and will benefit from accurate PAT systems with high sensitivity detectors.

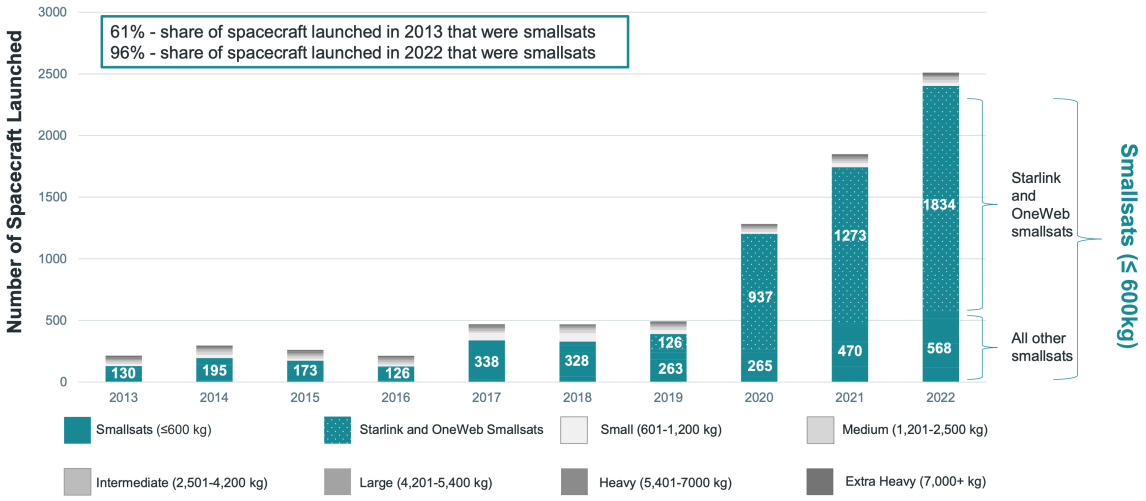

Figure 1-1: Spacecraft Launched 2013-2022, by Mass Class [2]

Small satellites, specifically CubeSats, are compelling platforms for novel technology demonstrations. Their small size and cost effective launches make them prime candidates for demonstrating and then implementing FSOC terminals. Their optoelectronics and optomechanical complexity is driven by the mission architecture and its distance, slew, stability, and data rate requirements. For many FSOC terminals, bulky mechanical gimbals are used. This thesis explores the possibility of further reducing the optical subsystem SWaP by using Silicon photomultipliers (SiPMs) as a dual communication and pointing sensor.

1.2 Communication Sensors

Photodetectors are optical sensors that transform an optical signal into an electrical current. The percentage of incident photons on the detector that are converted into electrons is defined as the photodetection efficiency (PDE). Most common photodetectors are silicon p-n junctions that leverage the photoelectric effect to generate an electron hole pair in the depletion region of the semiconductor, resulting in a photocurrent [3]. When operated in a reverse bias configuration with a high voltage, the electric field across the depletion region acting on the free charge carrier causes an avalanche current. The avalanche current is caused by the strong electric field forcing collisions between the photoelectron (p.e.) and other charge carriers in the valence band. If the electron hole pair collides with sufficient kinetic energy, the p.e. will generate secondary charge carriers, moving the electrons from the valence band to the conduction band. This is referred to as impact ionization, triggering an avalanche current. If the rate at which the free charge carriers are generated is lower than the rate at which they are collected (anode and cathode terminals), the avalanche is self-quenched. Typical amplification of p.e. to avalanche electrons, commonly known as gain, ranges from 10 to 1000. The high signal gain and linear scaling of a detected p.e. is what makes avalanche photodetectors (APDs) highly desirable in low power environments.

APDs that are operated above their breakdown voltage are called single photon avalanche photodetectors (SPADS). The detectors operate in a non-linear mode referred to as Geiger mode, where the rate at which free electrons are generated is greater than the rate at which the anode and cathode terminals can collect them. SPADs require a quenching resistor in order to stop the impact ionization by bringing the semiconductor below its breakdown voltage. The process of quenching highly restricts the efficiency of the detector at high frequencies. Other SPAD configurations address the issue of dead time (recovery time) by connecting several SPADs in parallel, forming a SiPM [4]. Even though each individual SPAD microcell is operated in Geiger mode and produces a full size avalanche from a single p.e., the SiPM overall behaves as a linear detector. Here the assumption is made that not more than one photon is incident per microcell per laser pulse. Due to the low noise in the system, the single p.e. can easily be amplified with a low-cost and low-power wideband IC amplifier. SiPMs have the benefit of the SPAD's high gain on the order of 10^6, while having a negligible dead time.

OnSemi created a SiPM configuration in which a "fast" output is generated in addition to the standard output. A capacitor is added to the SiPM output terminal of each microcell, effectively lowering the settling time of the avalanche by decoupling the output signal from the the quenching resistor and diode capacitances in the system [5]. This results in shorter dead times. Additionally, the SiPMs can be arranged in an array configurations where each SiPM with multiple microcells, referred to as a "pixel", is connected to other "pixels" through a common ground connection.

The fast response, high PDE, short dead time, low operating voltage and flexible geometry make SiPMs with a fast output a potential sensor for lasercom applications.

1.3 Pointing, Acquisition, and Tracking

Before communication is shared between an intersatellite link, both transmit and receive terminals go through a spatial acquisition routine to reach co-alignment. There are two principal spatial acquisition sequences according to the Consultative Committee for Space Data Systems (CCSD): beacon-based PAT and beaconless PAT [6] .

In the beaconless PAT sequence, both transmit and receive terminals go through open loop and closed loop stages. The open loop position estimate is based on the timing accuracy, position knowledge, attitude knowledge, disturbances, and planning cycles of each terminal. The accuracy of these parameters directly affects the open-loop misalignment between terminals, most commonly referred to as the uncertainty cone (UC). In order to reduce the UC after open loop pointing, the leader terminal emits light in a spiral pattern, and the follower terminal then decreases the uncertainty cone after each scan by adjusting its pointing direction. This processed is then repeated, but now with the leader and follower roles reversed.

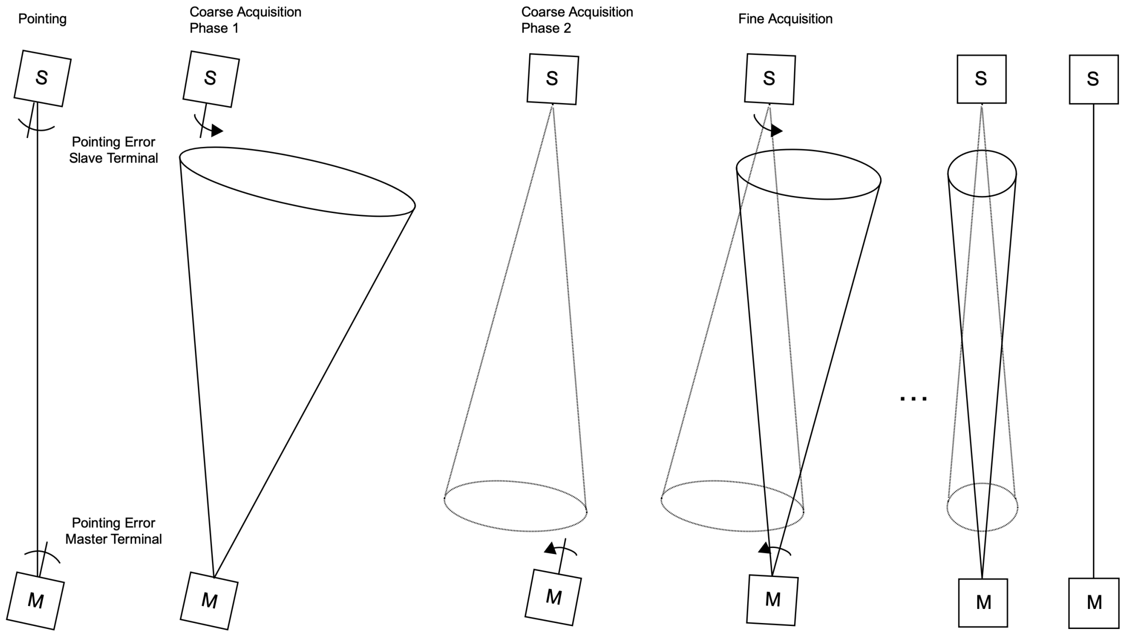

Figure 1-2: Beaconless PAT Sequence [6]

Once the UC reaches the mission pointing requirement, the tracking sensor is activated and the terminals are ready to establish an intersatellite link. This concept was first proved successful by the TerraSar-X Nfire optical links [6].

For beacon-based PAT sequences, a second transmit source with a larger beam divergence is used to encompass the uncertainty cone. A 2D sensor, such as a quadrant photodiode, measures the relative angular offset between the terminals. Section 2.1 describes the mechanism of the quadrant photodiode, or quadcell, in greater detail. The UC is reduced through a feedback loop by using the 2D quadcell sensor to measure the misalignment between the leader and follower terminals.

An example of a beacon-based acquisition sequence is the PAT procedure for the CubeSat Laser Infrared CrosslinK (CLICK) B/C mission. The CLICK-B/C mission is a technology demonstration of optical crosslinks with link distances ranging from 25 km to 580 km. In this mission, the pointing error is predicted to be less than 1.826 µrad [7]. This pointing error is achieved by separating the acquistion sequence in three stages: open loop tracking, closed loop coarse tracking, and closed loop fine tracking. The closed loop coarse tracking uses the beacon and a CMOS camera to measure the angular misalignment and is corrected by the spacecraft's body pointing control system. To further reduce the UC, the beacon light is focused by a Keplerian telescope onto a quadrant photodiode (quadcell), while being corrected by a Micro-Electro-Mechanical (MEMS) Fine Steering Mirror (FSM). The optical layout is shown in Figure 1-3.

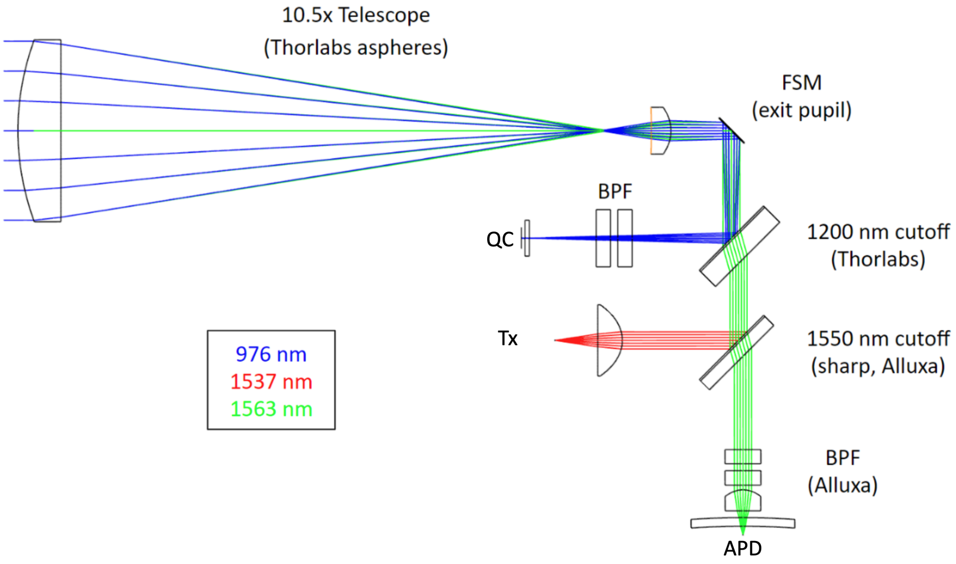

Figure 1-3: Beacon-based optical path diagram for the CLICK B/C mission. The beacon, transmit, and receive optical paths are depicted in blue, green and red, respectively [7].

All three signals share the same optical path into and out of the Keplerian telescope. Each signal is then redirected to their respective sensor using dichroic mirrors.

An interesting aspect of the beacon-based PAT systems is that the 2D position sensor can be used simultaneously for pointing and communication purposes, if it were able to support signal modulation detection at a high enough data rate.

1.4 Thesis Task Description

This research assesses the performance of SiPMs as dual communication and pointing detectors for FSOC LEO crosslinks. A set of requirements that are consisten with current technologies are specified. These requirements, such as bit error rate (BER) and crosslink distance, will drive the simulation and experimental design.

The pointing performance of a SiPM array architecture with a fast output is evaluated through simulations, and then corroborated with experimental results. It is of interest to model how different hardware metrics can modify pointing performance. The metrics of interest for this work include: beam diameter, beam power, cell size, and cell gap.

In this work we also develop electrical models that accurately simulate multiple microcells firing upon an incident light pulse. Current models are capable of simulating single cell avalanches [8], but lack the ability to scale to 100 or 1000s of cells without introducing circuit complexity. These models are used to predict sensor response upon receiving incident laser signals at different repetition rates. The simulation findings will then be compared to experimental results.

When the communication and pointing metrics are obtained for the SiPM, it is then possible to compare its predicted performance and SWaP to current LEO communication terminals, such as CLICK-B/C. We summarize both simulation and experimental results as well as introduce the scope for future work.

1.5 Organization of Thesis Sections

The following chapters of this thesis go through the approach, analysis, conclusions and future work of this research. Chapter 2 describes the approach taken to evaluate pointing and communication performance for a SiPM as well as the necessary equipment required for the experimental procedures. The test case for this technology is described in the last section of Chapter 2. In Chapter 3, the simulation and experiment designs are described. The results for pointing and communication test cases are presented in Chapter 4. Additionally, a study comparing the experimental and simulation results to current pointing and communication technologies is presented. Finally, in Chapter 5, the research is summarized and future work is discussed.

Chapter 2

Approach

For a SiPM to be implemented as a communications sensor in LEO while simultaneously updating misalignment between transmit and receive terminals, there are two major functions that it must be able to perform. The first function is to detect low power light pulses corresponding to 10s or 100s of incident photons at repetition rates greater than 1 MHz. The second function is measure the angular misalignment between terminals. This chapter explores possible ways to achieve this using a commercial-off-the-shelf (COTS) SiPM.

The communication performance of the detector is evaluated by testing its response to high repetition pulses at various power levels. The environmental conditions of the simulation and experiment are based on the optical link budget for a 1,000 km cross-link range in LEO. A model is used to simulate the response of a multi-cell detector at different repetition rates, accounting for noise in the signal. This model is then verified experimentally.

In order to detect angular misalignment with a SiPM, four different "pixels" are configured in a 2x2 geometry. Each pixel can be read independently. This configuration allows the SiPM to report the position of the beam relative to the center of the detector, which is then converted to an angular displacement. The angular sensitivity of the SiPM is first modeled and then tested experimentally.

For the COTS SiPM, in this work we use OnSemi's C and J SiPM series as they provide access to both a standard and fast output. The smaller pulse width of the fast output, also referred to as "fast axis", increases the maximum repetition rate detectable. This research focuses on obtaining the pointing and communication information from the fast axis.

2.1 SiPM Pointing Performance Overview

The COTS SiPM is used as a pointing detector by placing SiPM cells in a segmented quadrant position configuration. This geometrical configuration enables the SiPMs to report relative displacement of an incident beam in the x and y directions. The segmented quadrant configuration shown in Figure 2-1 is referred to as a quadcell, or QC.

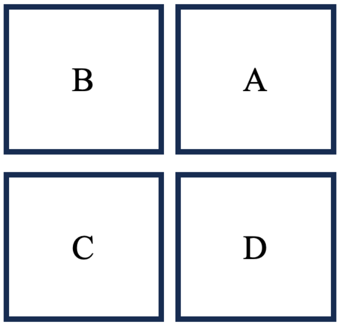

Figure 2-1: Quadcell geometry of 2x2 SiPM "pixels" organized into A, B, C, and D quadrants.

The relative displacement in the x and y directions is calculated using Equations 2.1 and 2.2, respectively;

$$x_{quad} = \frac{(A+D)-(B+C)}{(A+B+C+D)} \tag{2.1}$$

$$y_{quad} = \frac{(A+B)-(C+D)}{(A+B+C+D)} \tag{2.2}$$

where A, B C, and D are the measured signals by each SiPM pixel. The relative displacement is converted into an angle by placing a lens between the incident light and the detector, as shown in Figure 2-2,

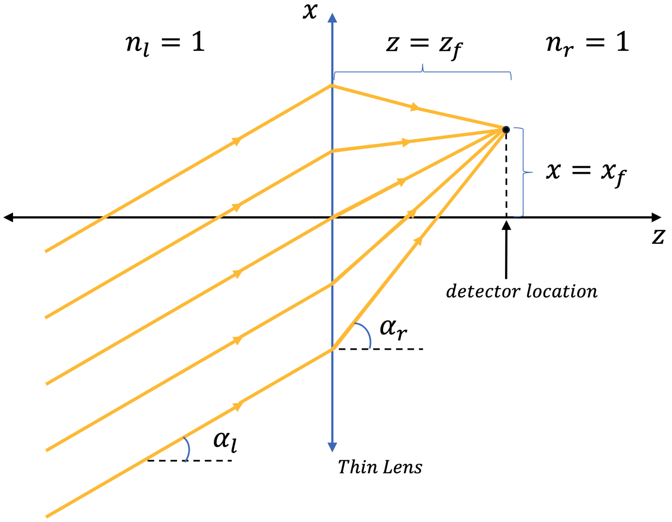

Figure 2-2: Plane wave incident on thin lens in air.

where n_l and n_r are the indices of refraction to the left and to the right of the lens, respectively. The focal length, f, occurs at $z = z_f$ with a lateral displacement of $x = x_f$, representing the point where all the incident rays converge.

The change in angle of incidence on the lens, a_l, results in a lateral displacement, x_f, as shown by Equation 2.3

$$\alpha_l = \tan\frac{x_f}{z_f}\ . \tag{2.3}$$

The system is assumed to be diffraction limited, meaning that the minimum detected angle is related to the wavelength of the light source, the width size (diameter) of the incident aperture, as well as the focal length of the system.

2.2 Tools Used for Pointing

The SiPM detector tested is the ARRAYJ-30035-16P-PCB, shown in Figure 2-3. It's a scaled up array consisting of 16 individual 3x3 mm^2 J-Series sensors. Each pixel is made up of 5,676 microcells, and each microcell has an area of 35 µm^2. The 20-way connector provides access to 16x standard I/O connections, 16x fast output connections, and 8x common ground connections. Table 2.1 presents a summary of the performance parameters.

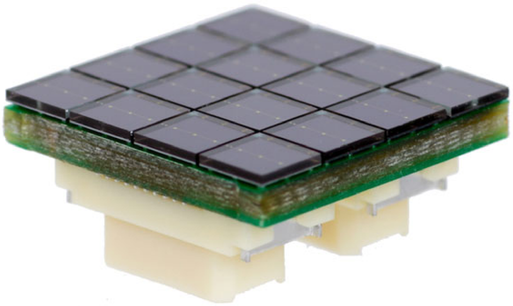

Figure 2-3: ARRAYJ-30035-16P-PCB (4X4 array of 3mm pixels) [9]

The signal connection diagram at the pixel level is shown in Figure 2-4. Each SiPM "pixel" is depicted as a photodetector connected by a common ground, where S_n represents the standard output and F_n the fast output.

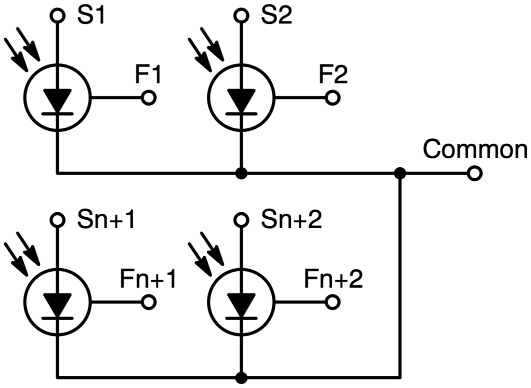

Figure 2-4: SiPM signal connections at the pixel level [9].

A COTS evaluation board manufactured by OnSemi is used to interface with the standard and fast outputs of the J-Series SiPM Array. The avalanche current triggered in the SiPM array is sampled from the fast output by a MDO4104C Tektronix oscilloscope. The oscilloscope has a bandwidth of 1 GHz and a maximum sampling rate of 5 GS/s [11]. The voltage measured in each of the four chosen pixels is then converted into a relative displacement in

Table 2.1: J-Series SiPM Sensor Parameters [10]

	Overvoltage		Unit
Parameter	+2.5V	+6V	V
PDE	38	50	%
Dark Count Rate	50	150	kHz/mm$\hat{2}$
Gain (anode-cathode)	2.9×10^6	6.3×10^6	
Dark Current - typical	0.23	1.9	uA
Dark Current - maximum	0.31	3	uA
Rise Time	90	110	ps
Microcell Recharge Time	45	45	ns
Fast Output Pulsewidth (FWHM)	1.5	1.5	ns
Crosstalk	8	25	%
Afterpulsing	0.75	5	%

the x and y direction.

An avalanche is triggered in each pixel by pulsing a laser beam on the detector. Thorlab's NPL45B nanosecond pulsed laser is chosen as the laser head. It has an adjustable pulse width, repetition rates up to 10 MHz, and a center wavelength of 450 nm. Its peak power is 75 mW with a max pulse energy of 3 nJ.

Figure 2-5: Nanosecond Pulsed Laser Diode [12]

The pulsed laser characterizes the pointing performance at different repetition rates. A range of link distances are replicated experimentally by attenuating the laser power using natural density (ND) optical filters.

In order to test the SiPM's angular sensitivity, a fast steering mirror (FSM) is used to introduce angular disturbances. Thorlab's GVS012 dual axis scanning galvo system is chosen to control the laser beam angle relative to the SiPM.

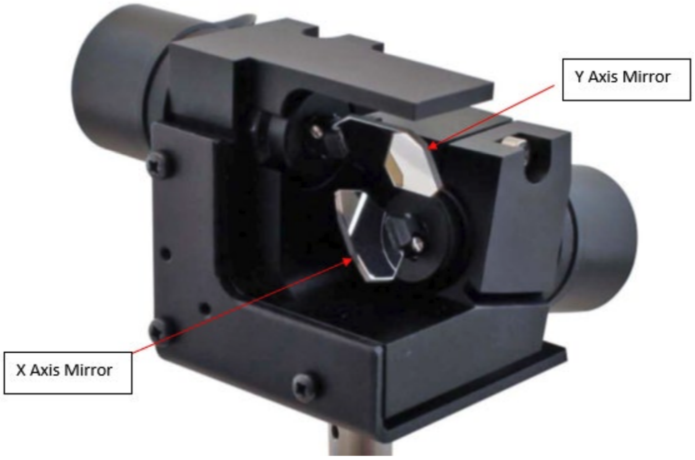

Figure 2-6: GVS012 Dual Axis Galvo/Mirror Assembly [13]

Each galvanometer assembly consists of a motor and a mirror attached at the shaft. The acceleration of the motor is controlled by the current applied to the motor coils. If the polarity of the current supplied is reversed, then the motor will come to a stop. The key specifications for the GVS012 system are shown in Table 2.2.

Table 2.2: Galvanometer GVS012 Parameters [13]

Beam Diameter	10 mm (Max)
Repeatability	15 µrad
Scan Angle	20°
Bandwidth Full Travel	25 Hz Square Wave
Small Angle Bandwidth	1 kHz
Small Angle Step Response	400 µs

A resolution of 15 µrad is possible if the recommended GPS011 Linear Power supply is used. Otherwise, the maximum achievable resolution is around 70 µrad. The GPS011 long lead time prevented its use for this application.

The angular disturbance actuated by the galvos is validated by a lens and camera setup, where the centroid location measured by the camera is translated to an angular displacement. A CMOS type sensor with a high PDE matching the laser wavelength is chosen to validate the angular disturbance in the system. Table 2.3 summarizes the parameters for the IDS Camera.

Table 2.3: IDS Camera Parameters [14]

Sensor Type	CMOS Color
Shutter	Rolling Shutter
Resolution	10.55 Mpix
Aspect Ratio	4:3
ADC	12 bit
Color Depth	12 bit
Pixel Size	1.67 µm
Optical Size	6.413 mm x 4.589 mm

Finally, a 50/50 beam splitter is placed in front of the FSM, dividing the incoming laser beam into two different optical paths with the same disturbance properties. The beam incident on the SiPM is first centered by minimizing the reported x_{quad} and y_{quad} values. The pixel location of the incident beam measured by the camera serves as a reference point from which the beam displacement is measured. As disturbances are introduced in the system by the FSM, both the quadcell and camera can measure the change in angle of the incident beam.

This configuration provides freedom to modify test parameters with ease, such as the power attenuation, pulse repetition rate, and scan angle. The primary goal of this setup is to provide insight into the SiPMs behavior as a pointing detector, with the noise equivalent angle (NEA) as the metric of interest.

2.3 SiPM High-Speed Pulsing Performance Overview

2.3.1 Link Budget for On-Off Keying Modulation Schemes

The SiPM's fast output signal pulsewidth is reported to be in the order of 1 ns [9]. Such a short pulsewidth may be leveraged to detect communication signals at high repetition rates. In this scenario, information is transmitted via a laser beam to the SiPM as a series of high or low power pulses. This modulation scheme is known as on-off keying (OOK), where a pulse of light with enough energy triggers an avalanche current in the SiPM and is interpreted as a logic high. A logic low corresponds to a period of time where the laser does not emit light. For this modulation scheme, the SiPM's response to a pulsed laser may be interpreted as a bit stream of data

The low dark count rate combined with a high PDE allows the SiPM to measure signals at low power levels. The lowest detectable power is dependent on the signal to noise ratio (SNR). In order to find the required minimum power that triggers an avalanche in the detector, a goal bit error rate (BER) for OOK modulation scheme is first established. A BER is defined as the rate of bits incorrectly received to total bits received. It is is related to SNR using Equation 2.4 [15],

$$BER = \frac{1}{2} erfc(\sqrt{SNR}) \tag{2.4}$$

where erfc is the complementary error function. The main sources of noise in photodetectors contributing to the SNR are: thermal noise, shot noise, and dark count noise [16]. For the COTS SiPMs used in this work, the main source of noise is assumed to be shot noise, as shown in Section 3.1. Shot noise is defined as the square root of the number of photons incident on the detector. The SNR for a shot noise limited system is defined as [17]:

$$SNR = \frac{N_{photons}}{\sqrt{N_{photons}}} = \sqrt{N_{photons}} \tag{2.5}$$

where $N_{photons}$ is the number of photons incident on the detector. By choosing a desired modulation type and BER, the required number of photons is calculated using Equations 2.4 and 2.5.

The total number of photons is translated to a required power at the detector by first evaluating the energy per photon, scaling it by $N_{photons}$, and then dividing it by the transmit terminal's, Tx, repetition rate to obtain an average power.

Planck's formula [18], Eq. 2.6, is used to calculate the photon energy, where c is the speed of light, h is Planck's constant, and λ is the wavelength of the Tx laser.

$$E = \frac{hc}{\lambda} \tag{2.6}$$

The optical power of the Tx necessary to achieve this BER is determined by calculating the optical path loss for a link distance of 1000 km.

The power loss in an optical crosslink is attributed to the beam's divergence. The transmitted beam is assumed to be in a standard transverse Gaussian mode. For a beam waist radius, w_0, the evolving beam width is calculated using Equation 2.7 [19].

$$w(z) = w_0 \cdot \sqrt{1 + \left(\frac{\lambda \cdot z}{\pi \cdot w_0}\right)^2} \tag{2.7}$$

The mathematical expression for the irradiance of the transverse electromagnetic mode as a function of z, the propagation distance, and r, the radial distance from the center of the beam, is shown in Equation 2.8,

$$I(r,z) = I_0 \left(\frac{w_0}{w(z)}\right)^2 \cdot exp\left(\frac{-2r^2}{w(z)^2}\right) \tag{2.8}$$

where I_0, the intensity of the beam at its waist, is defined by:

$$I_0 = \frac{2P_0}{\pi w_0^2} \ . \tag{2.9}$$

Substituting Equation 2.9 into 2.8, we obtain an expression for the irradiance of a Gaussian beam with units of W/m^2 in terms of the total power of the beam, P_0, the radial distance, r, and the beam width, $w(z)$.

$$I(r,z) = \left(\frac{2P_0}{\pi w(z)^2}\right) \cdot exp\left(\frac{-2r^2}{w(z)^2}\right) \tag{2.10}$$

The path loss is calculated by taking the ratio of $I(r,z)/I_0$. Converting to decibels is useful when calculating a link budget for ease of adding link range losses and system losses.

$$\frac{I(r,z)}{I_0} = \left(\frac{w_0^2}{w(z)^2}\right) \cdot exp\left(\frac{-2r^2}{w(z)^2}\right) \tag{2.11}$$

This power loss relation is used to generate an optical link budget for different link distances. The number of incident photons derived from the BER at a specific repetition rate is converted into a required transmit power.

2.3.2 Simulation of SiPMs with Varying Number of Microcells

The SiPM's response to a laser pulse with the conditions specified by the link budget is simulated and then tested experimentally. A circuit schematic is presented in Figure 2-7, where the standard output voltage can be read before or after amplification, (v_a and v_{out}).

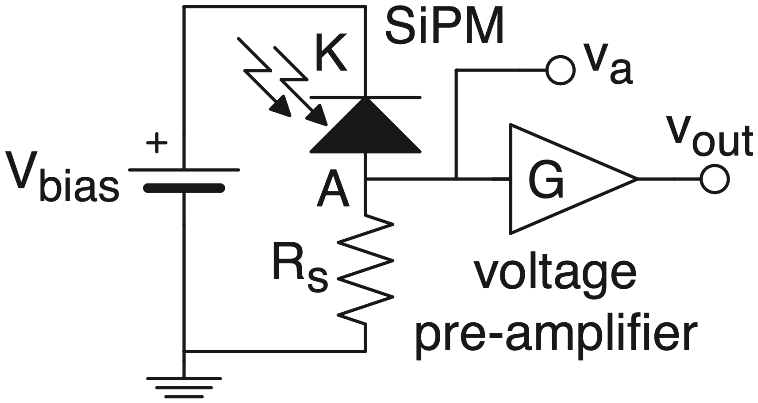

Figure 2-7: A SiPM biased above its breakdown voltage generates an avalanche current when light with sufficient energy is incident on the active area of the photodetector. The avalanche current flows through the shunt resistor, R_s. The standard output of the SiPM can be measured before or after amplification [8].

The electrical model of a SiPM was first introduced by [20], where the p-n junction of a microcell was modeled individually. A firing cell is represented by a current source in parallel with a diode capacitance, C_D, and a quenching resistor, R_q, in series. The results in [21] introduced the effects of grid capacitance, C_g, caused by the metal routing connecting the microcells in parallel. The accepted electrical circuit model for a SiPM shown in Figure 2-8 represents a single microcell firing. The rest of the non-firing cells, passive cells, are condensed through superposition analysis.

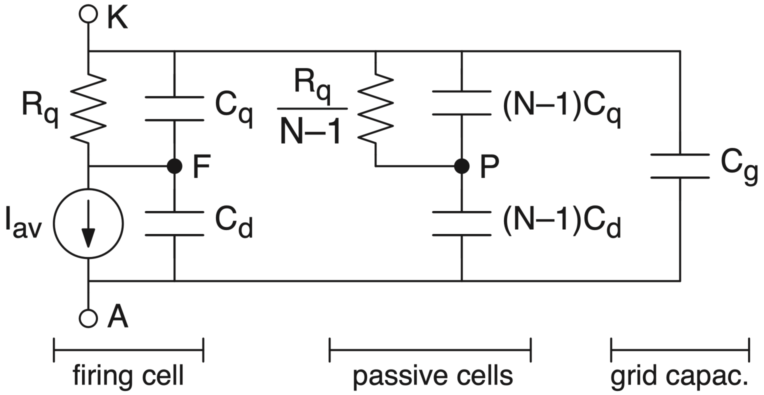

Figure 2-8: SiPM electrical model with N number of active and passive components [22].

A firing cell triggered by an incident photon generates an instantaneous avalanche current, I_{av}. This current is modeled as an ideal impulse by multiplying the charge released from the firing cell, Q_{av}, by the dirac delta function, δ_t, as presented in Equation 2.12 [8].

$$i_{av} = Q_{av} \cdot \delta(t) \tag{2.12}$$

Q_{av} is calculated by scaling the overvoltage, V_e, of the cell by the diode capacitance, C_d, as presented in Equation 2.13. The excess voltage, or overvoltage, is defined as the difference between the bias voltage, V_b, and the SiPM's breakdown voltage, V_{br}.

$$Q_{av} = V_e \cdot C_d \tag{2.13}$$

An array of firing cells presented in Figure 2-9 is discussed in [8]. The limiting factors of this model are the increased circuit complexity and simulation time, where each avalanche current needs to be parameterized individually.

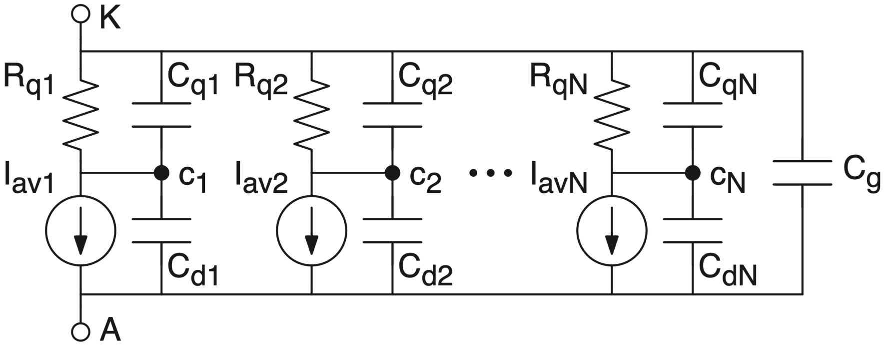

Figure 2-9: SiPM with N number of micro-cells. [8]

Assuming that the pulse of light on the SiPM triggers an avalanche in each microcell at exactly the same time allows the circuit in Figure 2-9 to be condensed. The result is shown in Figure 2-10. In this condensed model it is possible to simulate both firing cells, N_f, and passive cells, N_p.

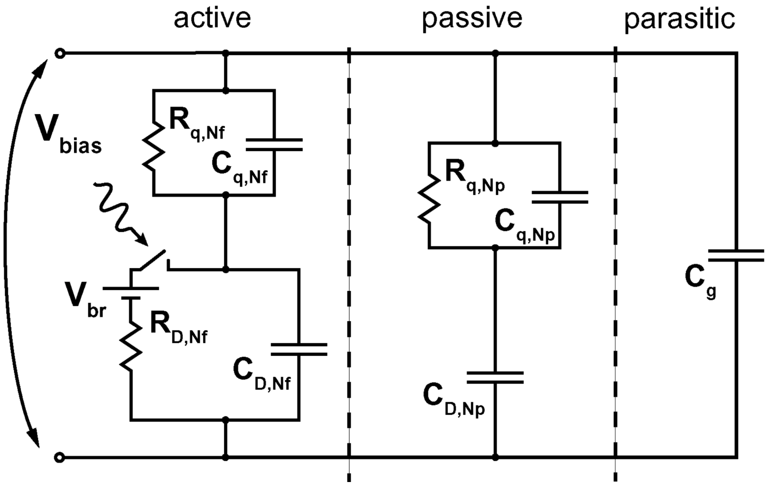

Figure 2-10: SiPM equivalent circuit for N_f firing cells and N_p passive cells[22].

A similar approach is taken to model the architecture of the COTS SiPM, specifically focusing on the response of the fast output and standard output.

2.4 Tools for Evaluating SiPM as a Communication Sensor

The ARRAYJ-30035-16P-PCB board is not used to detect high-speed pulses in this setup. Noise is introduced by the jumper wire connections to the fast output of each pixel. Instead, On-Semi's MicroFC-SMA-10035, shown in Figure 2-11, is evaluated for high frequency pulse detection. This single pixel SiPM has a sensor area of $1\,\mathrm{mm}^2$, with a total of 504 microcells. Each microcell has an area of $35\,\mu\mathrm{m}^2$. This PCB board provides three female SMA connectors for bias voltage, standard output signal, and fast output signal. The signal output connections are directly connected to the amplifier before being sent to the MDO4104C Tektronix oscilloscope for readout.

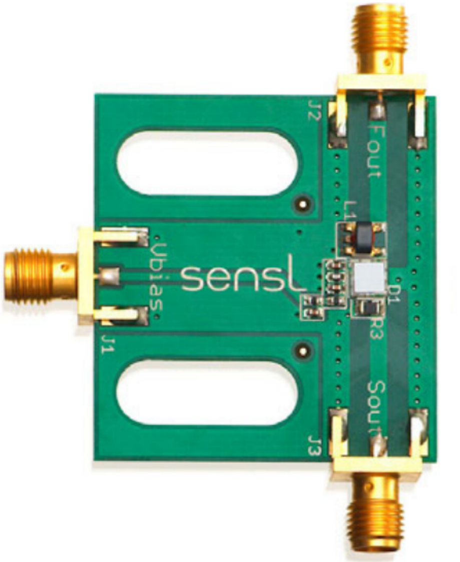

Figure 2-11: ARRAYC-10035 [23]

The board provides easy access to the standard and fast outputs, while maintaining timing performance. The ZFL-1000LN+ Low Noise Amplifier boosts the signal before it is read by the oscilloscope. The general layout of the experimental setup is presented in Figure 3-11 at the end of Section 3.4.

The high speed pulse is generated by PicoQuant's Sepia PDL 828 picosecond pulse driver and laser diode head. For the COTS SiPM, the maximum repetition rate is tested by increasing the pulse frequency of the laser driver. The Sepia PDL 828 laser driver generates pulses with picosecond widths at repetition rates up to 80 MHz.

Tables 2.4, 2.5, and 2.6 describe the parameters for the C-Series SIPM, the low power amplifier, and the pulsed laser.

Table 2.4: C-Series SiPM Sensor Parameters [23]

Parameter	Value	Unit
Min. Breakdown Votlage (Vbr)	24.2	V
Max. Breakdown Votlage (Vbr)	24.7	V
Min. Overvoltage	1.0	V
Max. Overvoltage	50	V
PDE	31	%
Peak Wavelength	420	nm
Dark Count Rate	50	kHz/mm^2
Gain (anode-cathode)	3×10^6	
Min. Dark Current	15	uA
Max. Dark Current	49	uA
Dark Count Current	3	nA
Rise Time	0.3	ns
Fast Output Pulse Width	0.6	ns
Microcell Recharge Time	5	ns

Table 2.5: Electrical Specifications for the ZFL Low Noise Amplifier[24]

Parameter	Frequency (MhZ)	Min.	Typ.	Max.	Units
Frequency Range		0.1			MHz
Noise Figure	0.1-1000	-	2.9	-	dB
Gain	0.1-1000	20	-	-	dB
Gain Flatness	0.1-1000	20	-	±5	dB
DC Supply Voltage		-	15		V

Table 2.6: Laser Diode Driver Head Specifications [25]

Wavelength [nm]	Pulse [PS]	Max rep rate [MHz]	High avg. power [mW]
640	<90	80	20

A low power environment is replicated by attenuating the power emitted by the Picoquant laser. An OD filter, with a transmission coefficient, T, is placed between the laser head and the SiPM. The power is attenuated to match the minimum number of photons at the SiPM that will result in a BER of 10^{-6}. This is achieved using a configurable ND filter.

Equation 2.14 shows the relationship between transmission T and OD factor.

$$OD = log_{10}\left(\frac{1}{T}\right) \tag{2.14}$$

The SiPM's fast axis response to different repetition rates is amplified and then processed by the oscilloscope before being saved to a data log. Increasing the repetition frequency of the laser pulses incident on the SiPM tests the pulse detection performance of the detector in a low power environment.

2.5 Test Case Overview

The performance of SiPMs as pointing and communication detectors is tested with the goal of eventually developing a high-speed lasercom system with micro-radian pointing resolution for smallsats in LEO. Platforms such as the CLICK-B/C satellites are ideal candidates that could benefit from this application. If SIPMs can successfully report pointing misalignment while simultaneously receiving data streams, the overall SWaP of lasercom terminals could decrease substantially.

Combining the pointing and communication sensors into a single component eliminates the need for a beacon laser, reducing the power requirement of the system. Additionally, the probability of the lasercom terminal being impacted by optical misalignment is reduced. This is shown by comparing the optical circuit footprint of the CLICK-B/C system to a SiPM based system. The top view of CLICK-B/C's optical platform is shown in Figure 2-12.

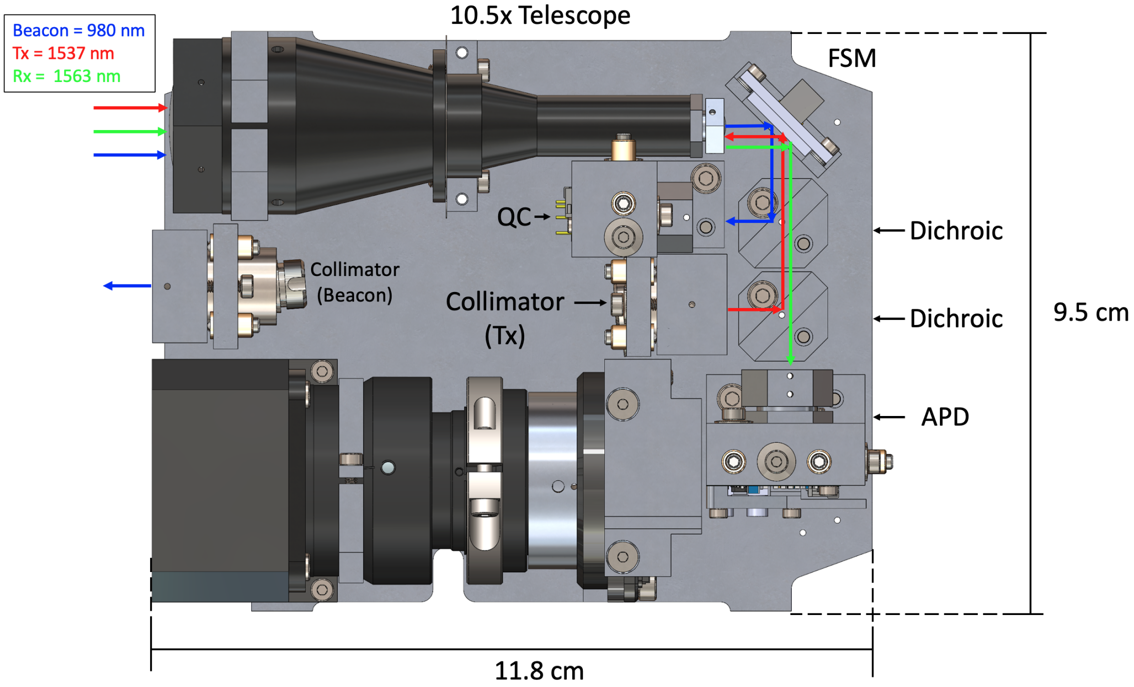

Figure 2-12: Top View of CLICK-B/C

The CLICK-B/C mission is capable of achieving data rates higher than 20 Mbps for link distances ranging from 25 km to 580 km. The B and C satellites are able to align before transmitting data by going trough the coarse and fine PAT sequences. These sequences start after the two satellites have finished body pointing using GPS coordinates. Coarse PAT uses the 980 nm beacon laser and the onboard camera to align both satellites by measuring angle misalignment and reporting it back to the spacecraft bus.

When the alignment meets the required angle, the fine PAT sequence begins. The quadcell detector reports misalignment at an update rate of 1 kHz, and the FSM corrects for this error. At this moment, data transfer begins by emitting light from the Tx collimator that is detected by the InGaAs APD. The beacon, transmit, and receive optical paths are aligned to each other in order to maximize power received at the APD.

The proposed application of the SiPM as a dual pointing and communication sensor simplifies the architecture needed for coarse and fine PAT sequences. Since the SiPM is capable of obtaining the data and misalignment angle from the same Tx beam for both coarse and fine PAT sequences, the onboard camera and beacon transmitter are no longer needed. The proposed architecture is presented in Figure 2-13.

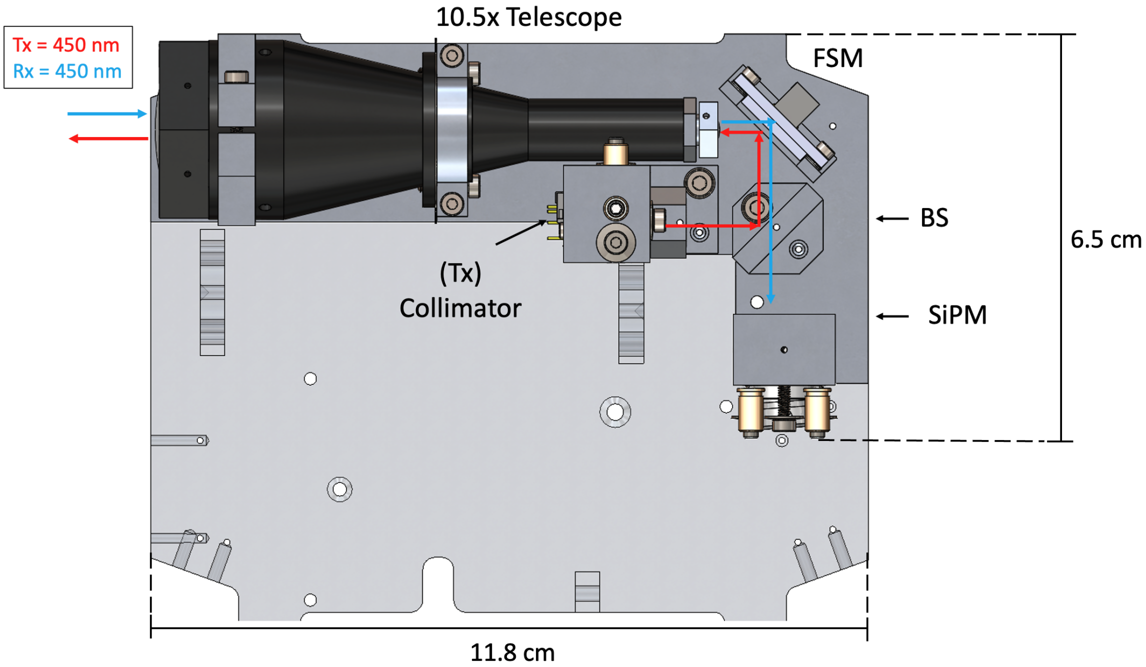

Figure 2-13: Top View of CLICK-B/C implementing SiPM as a dual pointing and communications detector.

Chapter 3

Analysis

This chapter presents the simulation models and experimental setups used to evaluate the pointing and high-speed pulse detection performance of the SiPM. Case 1 presents a parametric model of 4 SiPM pixels arranged in a quadcell configuration to characterize the NEA at variable pixel gap lengths, laser beam diameters, and pixel sizes. Case 2 describes the pointing experiment design implemented to corroborate the results from the pointing simulation. Case 3 introduces a new circuit modeling approach which simulates the standard and fast output responses of a SiPM to laser pulses at different repetition rates. Case 4 shows the experimental setup that tests the fast output response of a COTS SiPM at repetition rates up to 80 MHz.

3.1 Case 1 - Pointing Simulation

The pointing performance of a SiPM sensor is first evaluated by simulating the response of a quadcell SiPM pixel array to a scanning beam. The simulation outputs the relative position of the beam, dx and dy, measured by the SiPM as well as the NEA.

The SiPM quadcell is modeled after OnSemi's ARRAYJ-30035-16P-PCB. Each cell has an active area of 3 mm^3 and a gap of 200 µm. The quadcell model assumes a fill factor of

100%. Figure 3-1 shows the quadcell model, where yellow represents the active area of the sensor and blue the non-active area. Both cell size and gap width are parameterized in the simulation in order to model various SiPM geometries. For this simulation, the A, B, C, and D quadrants correspond to $(+x, +y)$, $(-x, +y)$, $(-x, -y)$, $(+x, -y)$ respectively.

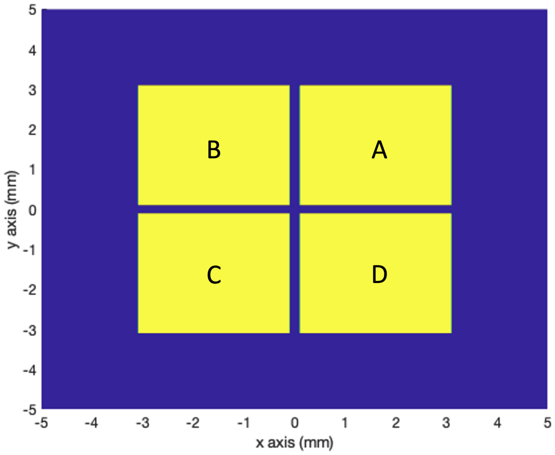

Figure 3-1: Model of ARRAY-J-30035 SiPM in a 2x2 pixel configuration.

The focused beam incident on the quadcell is modeled as a first order Bessel function, shown in Figure 3-2. The Bessel function is normalized by the total number of photons per pulse. The beam's intensity and diameter are adjustable to model different laser sources.

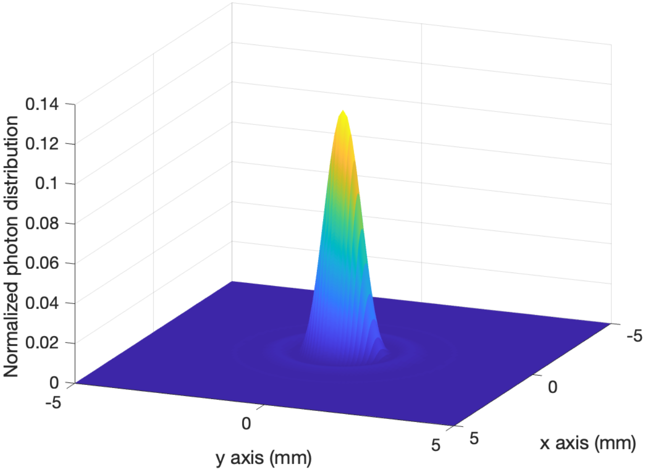

Figure 3-2: Laser beam modeled as a first order Bessel function.

In order to evaluate the sensitivity of the quadcell at different beam angles, the simulation scans the beam across the quadcell's diagonal from $(-x, -y)$ to $(+x, +y)$ and from $(-x, +y)$ to $(+x, -y)$. At each scanning step, the position of the beam on the quadcell is calculated using Equations 2.1 and 2.2. The sensitivity of the detector is then calculated by differentiating the reported positions, x_{quad} and y_{quad}, over the incident beam angles. The sensitivity of the quadcell to the beam scanning from one quadrant to another is dependent on beam diameter and pixel-to-pixel gap size.

$$s_x(x,y) = \frac{\partial x_{quad}}{\partial x}, \quad s_y(x,y) = \frac{\partial y_{quad}}{\partial y} \tag{3.1}$$

The smallest detectable change in angle by the quadcell is dependent on the noise in the system. Once the sensitivity of the SiPM is evaluated for different beam angles, Equation 3.2 is used to calculate the NEA [26],

$$NEA(\theta_x, \theta_y) = \frac{1}{f_{PT} \cdot SNR} \sqrt{\frac{1}{S_x^2} + \frac{1}{S_y^2}} \tag{3.2}$$

where SNR is the signal to noise ratio and f_{PT} is the focal length of the beam incident on the quadcell. Since the sensitivity of the sensor relates a change in beam position to a reported x_{quad} position, it is necessary to divide by f_{PT} in order to obtain an angular relation. The NEA is evaluated for various beam spot sizes, quadcell gap sizes, and power levels of laser pulses incident on the detector.

The SNR represents the minimum detectable signal in the system with noise present, as shown in Equation 3.3,

$$SNR(x,y) = \frac{N_A + N_B + N_C + N_D}{\sqrt{\sigma_A^2 + \sigma_B^2 + \sigma_C^2 + \sigma_D^2}} \tag{3.3}$$

where the main components of the noise, σ_{pixel}, are shot noise, σ_{shot}, dark noise, σ_{dark}, and thermal noise, $\sigma_{thermal}$ [16].

$$\begin{aligned}
\sigma_{pixel}^2 &= \sigma_{shot}^2 + \sigma_{dark}^2 + \sigma_{thermal}^2 \\
\sigma_{shot}^2 &= 2qI_{shot} \\
\sigma_{dark}^2 &= 2qI_{dark} \\
\sigma_{thermal}^2 &= \frac{4kT}{R_L}
\end{aligned} \tag{3.4}$$

Shot noise is calculated by multiplying electron charge, q, by the current generated by the signal optical power, I_{shot}, which is proportional to the number of incident photons, $N_{photons}$. Dark noise is caused by dark counts, N_{dark}, triggering in dark conditions and generating a dark current, I_{dark}. The dark counts can be calculated by dividing the dark count rate of the sensor by the frequency at which information is being sampled. Thermal noise, or Johnson noise, is dependent on the absolute temperature, T, the load resistance, R_L, and the Boltzmann constant, k [16]. Thermal noise in addition to electronic noise from the sampling system can be considered to be negligible for SiPMs, as reported by [27].

The overall NEA of the quadcell can be reduced by increasing the SNR using ensemble averaging. For this application, the pointing and communication signal update rates have different frequencies: f_{pntg} and f_{comms}. The number of samples that the pointing signal is averaged over depends on the ratio of both of these frequencies, as shown in Equation 3.5:

$$n_{ave} = \frac{f_{comms}}{f_{pntg}} \ . \tag{3.5}$$

Ensemble averaging is introduced as a noise reduction technique for spectroscopy and non-destructive testing in [28]. This same approach is used to increase the SNR in the pointing signal of the SiPM. The signal and variance are scaled as described in Equation 3.6.

$$\begin{aligned}
S_{n,av} &= \sum_{i=1}^{n} S_i = n_{av} \cdot S_i \\
\sigma_{n,av}^2 &= \sum_{i=1}^{n} \sigma_i^2 = n_{av} \cdot \sigma_i^2
\end{aligned} \tag{3.6}$$

The noise, N, is defined as the square root of the variance. The signal to noise ratio then becomes:

$$\left(\frac{S}{N}\right)_{n,av} = \frac{n_{av} \cdot S_i}{\sqrt{n_{av}} N_i} = \sqrt{n_{av}} \left(\frac{S}{N}\right)_i \tag{3.7}$$

An increase in n_{av} corresponds to an increase in the SNR for the pointing signal, further decreasing the NEA of the system. This is a unique advantage to sampling the output of the SiPM to calculate angular misalignment while receiving bit streams of data.

3.2 Case 2 - Pointing Experiment

The experiment mimics the power environment that the SiPM would encounter as a receive terminal and characterizes its performance as a pointing sensor. The crosslink distances of interest range from 500 km to 1000 km. This is achieved by attenuating the input optical power using OD filters.

OnSemi's ARRAYJ-30035-16P-PCB 4x4 pixel array is the COTS SiPM used for this experiment. The pointing performance of the COTS SiPM is tested by reading the standard output of two neighboring pixels, while a laser beam is scanned across the x axis. Two adjacent pixels are used for the pointing experiment instead of the typical 2x2 pixel configuration due to connection constraints in the evaluation board, where only two SiPM pixels can be read simultaneously.

In this experiment, the NPL45B laser is attenuated using OD6 natural density filters in order to simulate the minimum power necessary for the quadcell to accurately report a pointing disturbance in the x and y directions. The power attenuation of the laser results in 122 photons incident on the SiPM, which is close to the 100 photons required to achieve a BER of 10^6.

Laser light pulsing at 1 MHz is directed into the FSM mirror, where angular disturbances, θ_x and θ_y, are introduced into the system. A 50/50 beamsplitter is placed right after the

FSM, dividing the light into two beams, one incident on the quadcell and the other on the camera. A diagram of the experiment setup is shown in Figure 3-3. The camera is used as an instrument to validate the beam angle driven by the FSM. For each mirror step, the centroid location of the beam is obtained from a Gaussian fit of the image captured by the camera. The Gaussian fit is able to generate a beam centroid estimate with sub-pixel accuracy.

The FSM steers the pulsed light beam from the $-x$ to $+x$ with a step size of 60 µrad where the voltages of each pixel at each step are read and stored by the oscilloscope. Once the data for a complete sweep from -x to x is completed, the beam position reported by the quadcell is calculated based on the data captured.

Measurements of the beam location at each incident angle are then numerically differentiated using Equation 3.1, but in this scenario only with Pixels A $(+x)$ and B $(-x)$. The NEA of the SiPM is then evaluated.

The experiment showcases how a SiPM can be used in a quadcell configuration as a pointing detector for link distances of 1000 km while updating beam position up to 1 MHz. The experimental setup is shown in Figure 3-3.

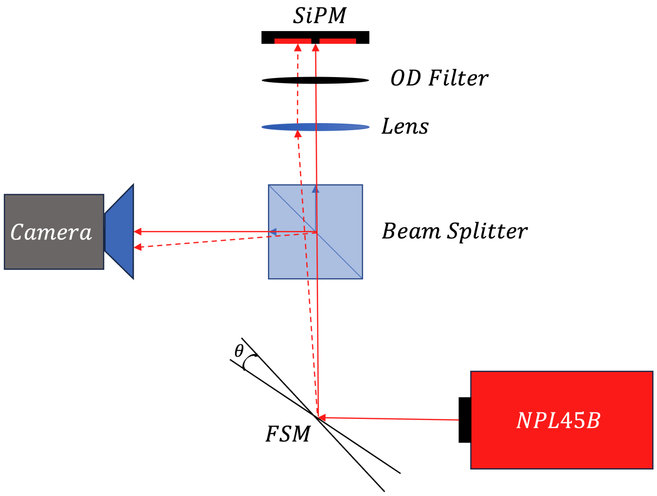

Figure 3-3: NEA Experimental Set-up

3.3 Case 3 High Speed Pulsing simulation

A novel approach to model the firing of SiPM cells is introduced in this section. The goal of the model is to simulate the avalanche current in the sensor triggered by low power pulses at high repetition rates.

First, the COTS SiPM architecture is used to simulate a standard and fast response. Reading a fast response is possible by attaching a capacitor at the node connecting the current source and the quenching resistor. The circuit schematic is shown in Figure 3-4.

Each individual microcell is modeled as a current source with a diode capacitance in parallel, and a quenching resistor in series. The quenching resistor, R_q, is modeled to have a quenching capacitance, C_q.

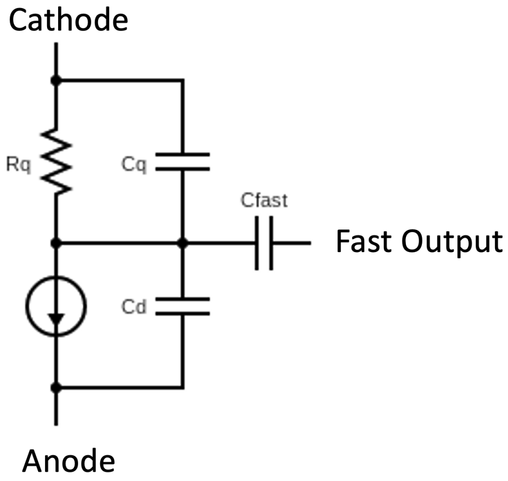

Figure 3-4: Microcell circuit schematic for reading the fast response of a SiPM.

Multiple cells are connected together to represent a SiPM with N microcells. The routing that connects the micro-cells together introduces a grid capacitance, C_g. These models quickly become cumbersome when the SiPM is made up of 100's or 1000's of cells.

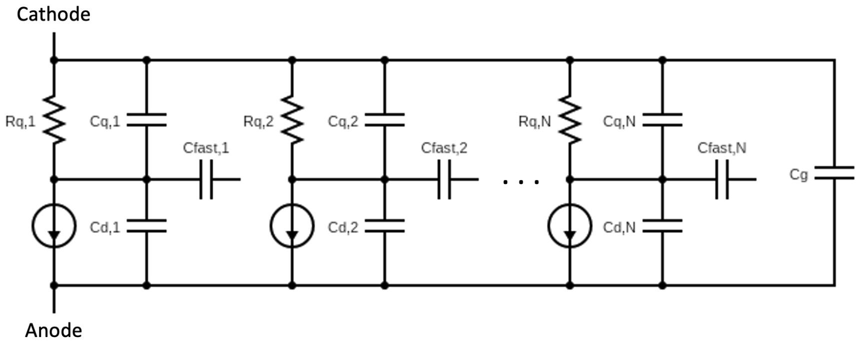

Figure 3-5: Microcell circuit schematic of a SiPM with N active cells before condensing.

To avoid circuit complexity, the schematic in Figure 3-5 is condensed by distinguishing between firing cells and passive cells. Firing cells are represented by an active current source that generates an impulse current for an infinitesimal amount of time. Passive cells are modeled as elements with no current flowing through them, resulting in an open circuit at their node location. By assuming that all firing cells trigger at the same time it is possible to simplify the circuit by combining impedances in parallel. Instead of having multiple current sources firing at various nodes, a single current source is triggered. The magnitude of the triggered current is proportional to the number of firing cells. The condensed schematic is shown in Figure 3-6.

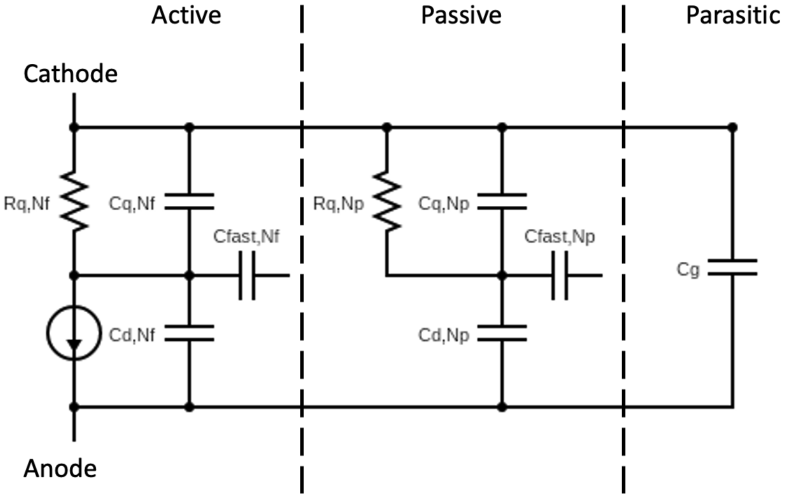

Figure 3-6: SiPM model with active and passive cells.

The impedances are defined in Equation 3.8, where N_p represents passive cells and N_f active cells.

$$\begin{aligned} R_{q,Nf} &= \frac{R_q}{N_f} & R_{q,Np} &= \frac{R_q}{N_p} \\ C_{q,Nf} &= C_q \cdot N_f & C_{q,Np} &= C_q \cdot N_p \\ C_{d,Nf} &= C_d \cdot N_f & C_{d,Np} &= C_d \cdot N_p \end{aligned} \tag{3.8}$$

This model is incorporated into a readout circuit shown in Figure 3-7. A shunt resistor is placed in series with the current source, which generates a measurable voltage drop when an avalanche current is triggered by incoming light. The voltage source sets V_{bias}, and affects the overvoltage across C_d.

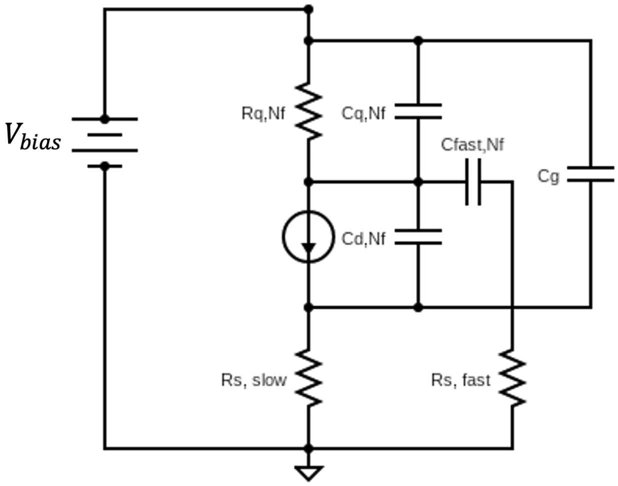

Figure 3-7: Readout circuit of C-series SiPM.

A symbolic expression of the voltage across the shunt resistor is obtained with superposition analysis. As a result, the V_{bias} is shorted, and the impedances are re-organized. In order to characterize the circuit's behavior to a current impulse, the current source and the impedances are represented in the frequency domain. This configuration allows for transfer function analysis at different nodes of interest, such as C_d, $R_{s,slow}$, and $R_{s,fast}$.

Figures 3-8 and 3-9 represent Norton and Thevenin equivalent circuits. In the Norton equivalent circuit, the transfer function derived relates the instantaneous avalanche current to the voltage across C_d. For the Thevenin equivalence, the same approach is followed.

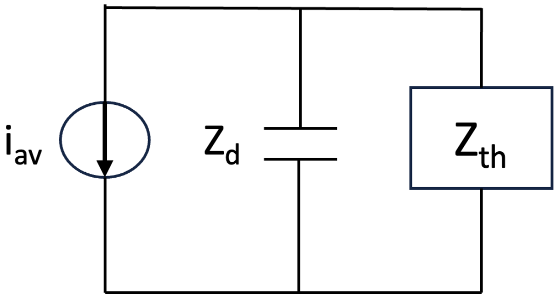

Figure 3-8: Norton Equivalent Circuit

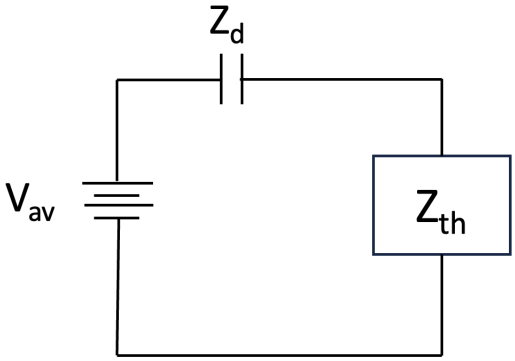

Figure 3-9: Thevenin Equivalent Circuit

When comparing the transfer functions it becomes apparent that an impulse response in the Norton circuit (Eq. 3.9) is equivalent to a scaled step response in the Thevenin Circuit (Eq. 3.10).

$$H(s) = \frac{Z_{th}}{sc_d \cdot Z_{th} + 1} \tag{3.9}$$

$$H(s) = \frac{Z_{th}}{sc_d \cdot Z_{th} + 1} \cdot sc_d \tag{3.10}$$

The avalanche current of a firing microcell in Equation 2.12, fed into the Norton Equivalent circuit produces an output voltage described by Equation 3.11.

$$V_{out}(s) = \frac{Z_{th}}{sc_d \cdot Z_{th} + 1} \cdot v_e \cdot c_d \tag{3.11}$$

A mathematically identical response is obtained from the Norton equivalent circuit when the input voltage is

$$V_{in}(s) = \frac{v_e}{s} \ . \tag{3.12}$$

This simplifies the model and removes the constraint of the simulation's step resolution. An avalanche simulated by an impulse is limited by the step size of the software. The simulation is built in Simulink, allowing variable inputs such as number of active microcells, overvoltage, and pulse repetition rate.

The COTS SiPM is assumed to be shot noise limited based on the low dark count rate reported. The shot noise of the signal follows a Poisson distribution. This distribution is modeled using Equation 3.13,

$$Pr(N = k) = \frac{e^{-\lambda t}(\lambda t)^k}{k!} \tag{3.13}$$

where λ represents the expected number of arrival photons for a specific time interval t. This distribution is used to create a probability density function (PDF) for the noise in the system.

Simulink provides a tool that generates values based on a PDF. This function is used to model noise in the SiPM current.

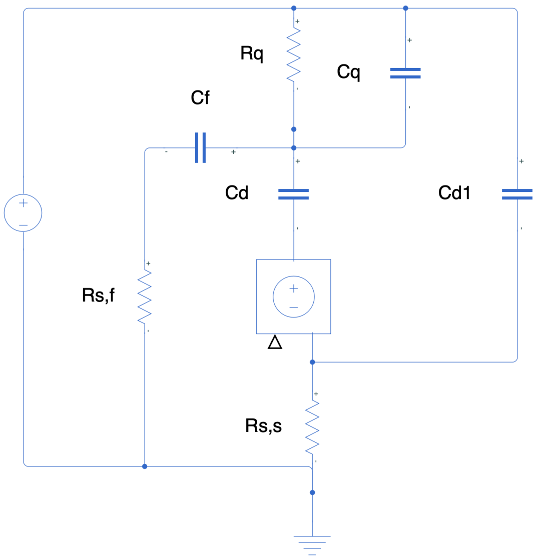

Figure 3-10: Readout diagram of condensed SiPM Thevening equivalent circuit in Simulink.

3.4 Case 4 - High Speed Pulsing experiment

OnSemi's ARRAYC-30035 SiPM is evaluated as a communication sensor by exposing it to high-speed pulses in a low power environment. This test evaluates the avalanche current signal properties, and predicts the theoretical repetition limit based on the signal's pulse width.

The layout of the experiment is shown in Figure 3-11. An avalanche current is triggered by incoming light from a picosecond pulsed laser which is focused by a lens onto the detector. The fast output of the SiPM is amplified and then converted to a digital signal by the oscilloscope. After the data has been captured for different repetition rates, it is exported to a computer and analyzed.

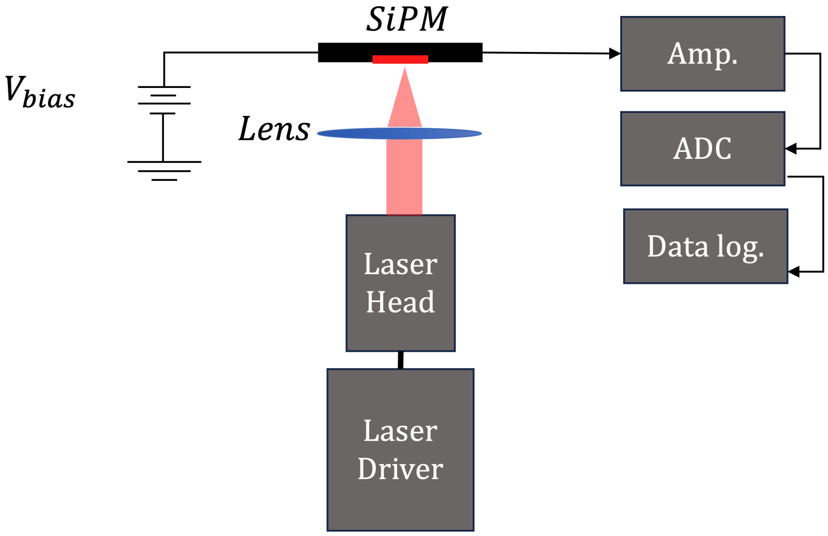

Figure 3-11: High Speed pulsing experimental setup.

For the experiment, a BER of 10^{-6} is set as a goal parameter. Using Equations 2.4, 2.5, and 2.6, the set BER is converted into an average incident power on the detector.

The picosecond pulsed laser has a high average power of 20 mW. A natural density filter array with a total $OD = 7$ attenuates the power to around 64 photons per pulse, close to our required number of photons N to achieve a BER of 10^{-6}.

The laser driver is then used to test the response of the SiPM to pulses with frequencies of 20 MHz, 40 MHz, and 80 MHz. This experiment showcases the performance of a SiPM when high speed pulses are sent as a communication signal. The modulation scheme used is OOK.

Chapter 4

Results

The simulation and experimental results of the SiPM's NEA and response to high-speed pulses are presented in this chapter. An optical link budget is is used to calculate the optical path loss for a link distance of 1000 km. This optical path loss establishes the transmit power required to achieve a BER of 10^{-6} for an OOK modulation scheme. An SNR analysis is then carried out to compare the dark count noise and the shot noise of the system when ensemble averaging is used as a tool to decrease the NEA of the SiPM.

Four subsections are presented in this chapter. Subsection 4.1.1 shows the results for the NEA simulation, providing insight into how the quadcell's gap length and beam diameter affect the pointing sensitivity of the detector. Subsection 4.1.2 reports the experimental results of the SiPM's angular resolution obtained from sweeping a laser across 2 different SiPM pixels. Subsection 4.1.3 presents the simulation results of the SiPM's standard and fast output using the proposed "condensed" model and compares it to the typical N-cell circuit model. The maximum predicted pulse rate detectable by the SiPM is corroborated by experimental results. Subsection 4.1.4 presents the SiPM's response to light pulses with repetition rates of 20 MHz, 40 MHz, and 80 MHz.

4.1 Findings from all Cases

For a communication system that is shot noise limited, the required number of photons at the detector is calculated based on a desired BER.

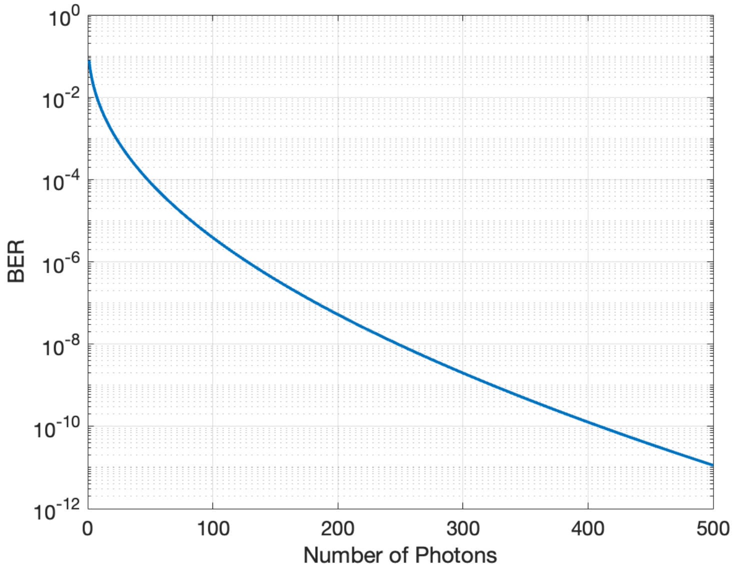

Figure 4-1: BER of OOK modulation for different noise levels.

Equation 2.4 is used to calculate BER for different SNR levels of a shot noise limited detector, where the SNR is equivalent to the square root of the number of incident photons. A desired BER of 10^{-6} corresponds to a total of 125 photons, which is decreased to 100 to be conservative and evaluate the system at a lower power level. This is taken as the initial estimate of required energy at the detector.

The optical path loss and required power at the transmit terminal are derived from the power link budget introduced in Section 2.3. The results for the optical link budget are presented in Table 4.1.

A total optical loss of -57 dB requires an average transmit optical power, P_{Tx}, of 17.6 mW in order for 100 photons to be incident on the detector.

Given a communication update frequency of 100 MHz and and pointing update frequency

Table 4.1: Optical link budget parameters with power losses presented in dB.

Parameter	Value	Units
λ_{laser}	450	nm
f_{Tx}	100	MHz
w_0	0.012	m
$Link\ range$	1,000	km
P_{tx}	17.6	mW
L_{Tx}	3	dB
L_{Rx}	3	dB
L_{SiPM}	3	dB
L_{Path}	-57	dB

of 1 kHz, an SNR evaluation is carried out for the COTS SiPM.

First, the shot noise of the signal is evaluated. For 100 incident photons in a shot noise limited system, the resulting shot noise and SNR is 10. The shot noise is intrinsic to the signal and is not affected by the SiPM update rate. On the other hand, the dark count scales linearly with the area of the detector and inversely with the update frequency. Figure 4-3 supports that for faster update frequencies, the system is shot noise limited.

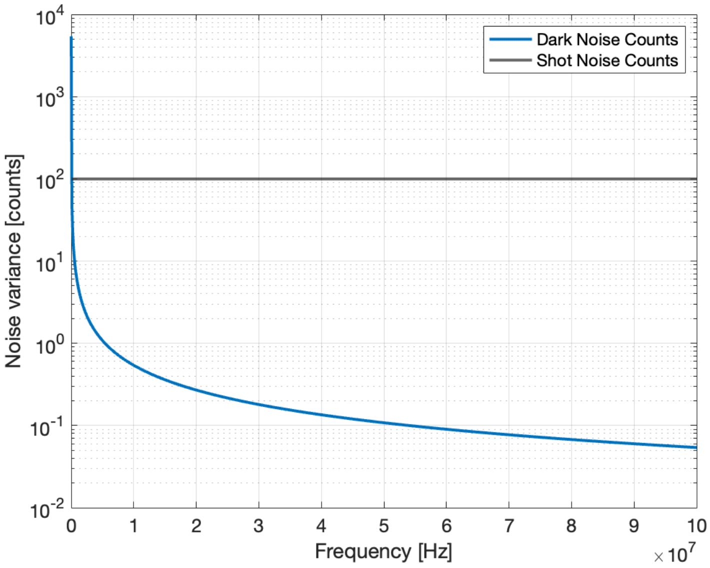

Figure 4-2: Noise per sample at different update frequencies

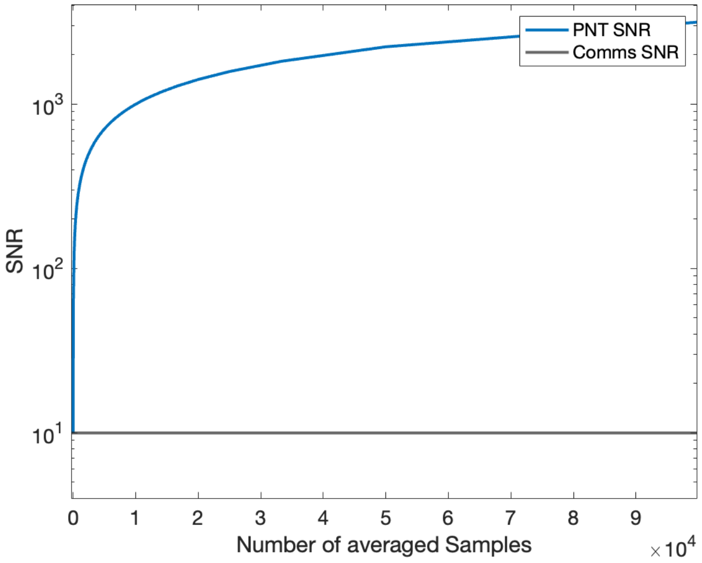

Figure 4-3: SNR at different number of averaged samples.

Following the ensemble averaging methodology, Figure 4-3 shows how the SNR for the pointing signal increases as the signal is averaged over a greater number of samples. The SNR of the communication signal does not change at different sampling rates because the shot noise is inherent to the optical signal. The greater the difference between f_{comms} and f_{pntg}, the smaller the NEA is for the SiPM.

From this analysis, we make the assumption that for the update frequencies of interest, the system is shot noise limited. This assumption will be explored further in future work by taking into considerations other factors such as crosstalk and afterpulsing.

4.1.1 SiPM Pointing Simulation Results

The experimental and simulation results presented in this subsection model the response of a 4 quadrant SiPM as a beam of light is steered across the x-axis. The quadcell response is modeled as the beam diameter increases each iteration. The gap length between the cells is fixed to 200 µm, driven by the physical characteristics of the J-Series SiPM. Figure 4-4 showcases the behavior of the reported position, x_{quad} for different beam diameters. The sensitivity of the SiPM for different beam diameters is presented in Figure 4-5.

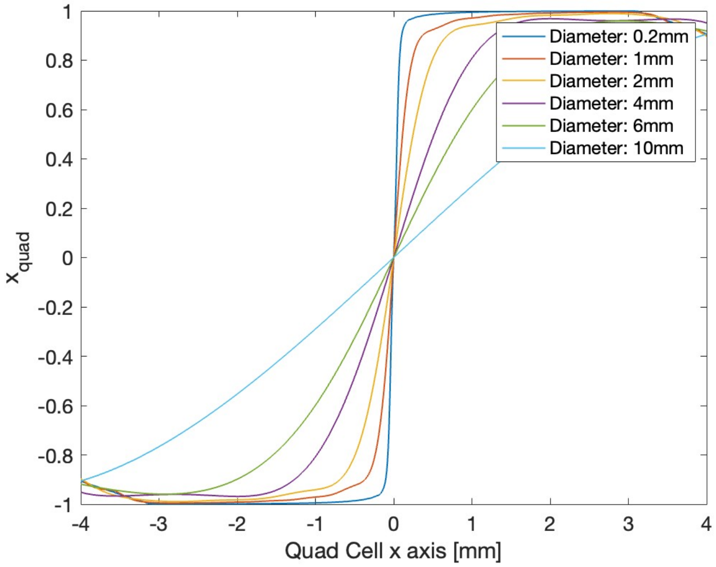

Figure 4-4: x_{quad} for different beam diameters as beam scans through the x axis.

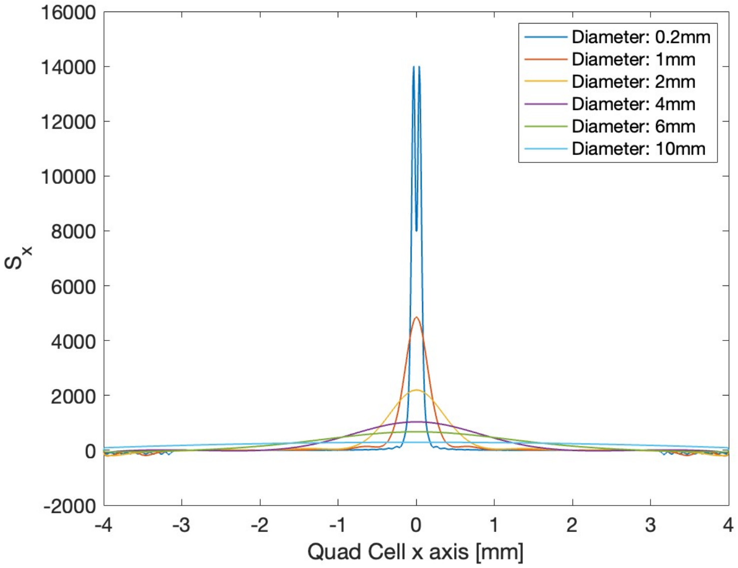

Figure 4-5: S_x for different beam diameters as a beam scans through the x axis.

A wider diameter beam results in a larger detectable range for pointing disturbances. This comes at the cost of flatter response, or lower angular resolution. A steeper slope represents a higher angular sensitivity.

The slope factor for each beam diameter is calculated and reported in Figure 4-5. In this plot, the magnitude of the slope increases as the beam diameter increases. Interestingly, even though the 200 µm diameter has the highest slope factor, it also has a dip right around the center of the quadcell. This occurs because the beam diameter is smaller than the gap length between the SiPM pixels of the quadcell. If the beam diameter is smaller than the gap length, the quadcell is unable to provide a relative position estimate.

A similar analysis is carried out to characterize the angular resolution of the SiPM in response to the gap size between the quadrants of the quadcell. The model decreases the gap length each iteration while fixing the beam diameter to 200 µm. Figure 4-6 presents the results for a variable gap length.

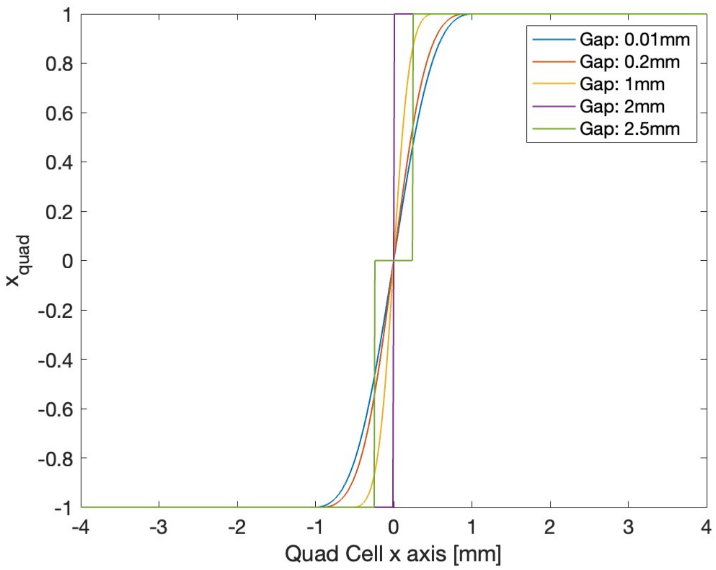

Figure 4-6: S_x for different gap lengths as a beam scans through the x axis.

Smaller gap lengths allow for more light to be captured by the pixels in the quadcell. This means that the SiPM is capable of reporting a relative position to the center for smaller gap lengths. As the gap increases for a fixed beam diameter, there is a sharper transition from the -1 to 1 reported position states. If the beam diameter is smaller than the gap, then the quadcell would fail to center the incoming beam disturbance. Figures 4-7 and 4-8 highlight the sensitivity of the SiPM for various pixel gap lengths.

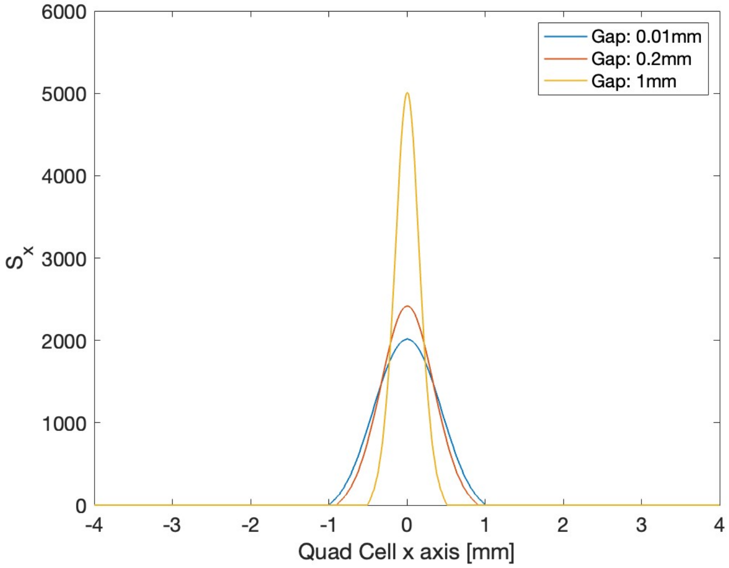

Figure 4-7: S_x for smaller pixel gap lengths.

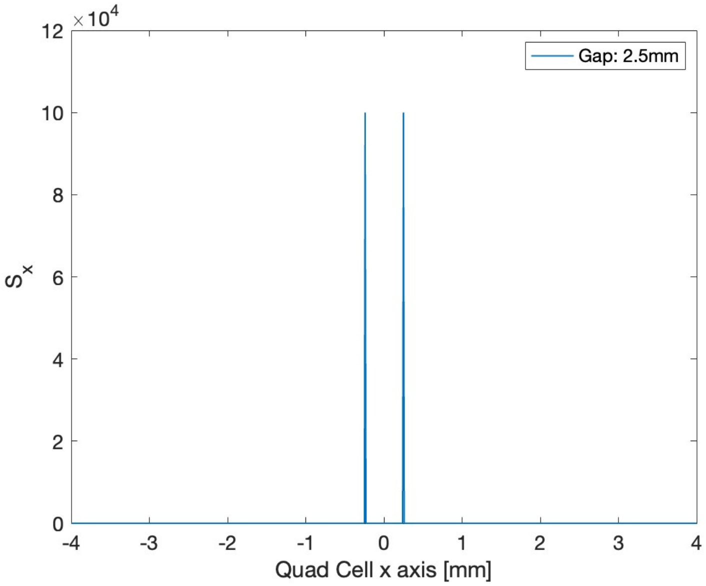

Figure 4-8: S_x for a gap length larger than the beam diameter.

For a gap length of 2.5 mm there is a sharp transition in the reported x_{quad} from -1 to 0. This happens because the beam transfers from the $-x$ quadrant to the gap. The beam then shifts trough the gap, reporting zero relative position, up until it reaches the $+x$ quadrant. The angular resolution is limited by the gap region in this scenario. The two spikes in Figure 4-8 represent the sudden transition when the beam enters the gap region and leaves it. The slope factor decreases to zero in the region.

There is a compromise between the maximum angular sensitivity and the reported angular range of a quadcell. The dynamic range of the SiPM depends largely on the sizing of the beam diameter relative to the gap length between quadrants. If the system requirements dictate a wide range of angles, then a wide beam relative to gap length and pixel size is preferable.

4.1.2 SiPM Pointing Experiment Results

The behavior of the SiPM as a pointing detector is tested experimentally by scanning the Array-J-Series detector with a steering mirror as introduced in Section 3.1. The beam of light incident on the detector is attenuated using an OD6 filter in order to generate the adequate amount of energy (122 photons). In this test, the laser is pulsed at a rate of 1 MHz.

As the beam scans along the x axis, the voltage at the A and B pixels is measured with an oscilloscope. At each sweep step the x_{quad} location is calculated using Equation 2.1.

Figures 4-9, 4-10, and 4-11 depict the voltages measured by each pixel at different beam locations.

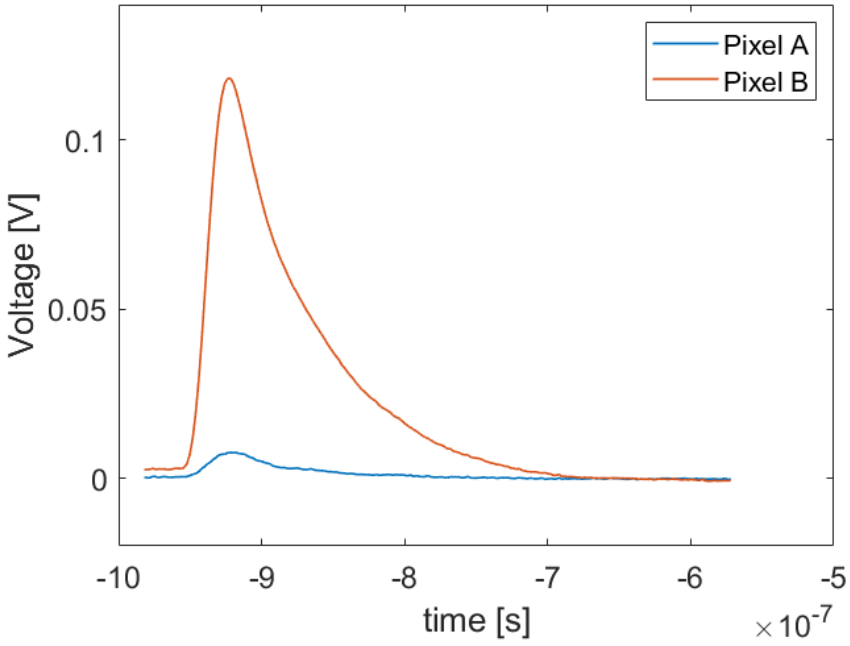

Figure 4-9: Pixel A and B Voltages for $x_{quad} = -0.9115$

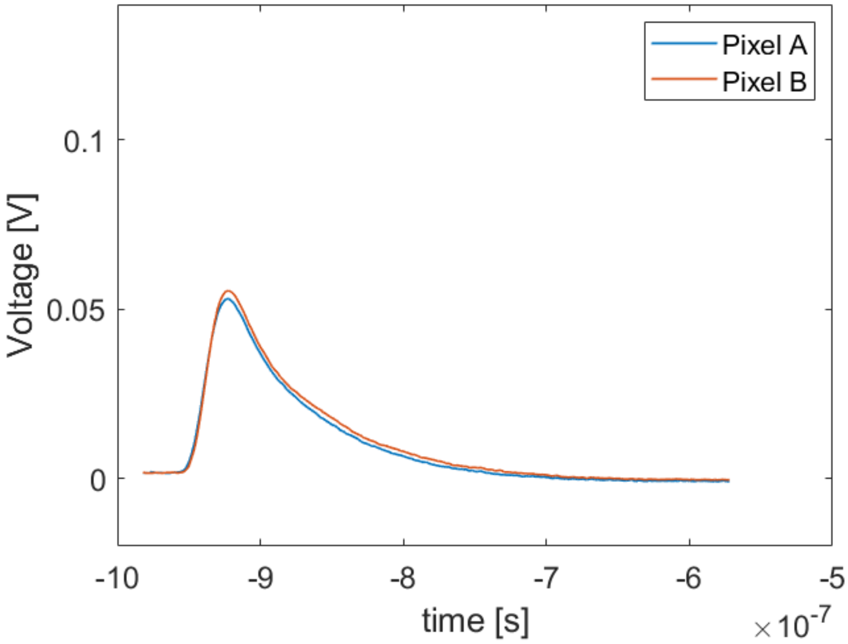

Figure 4-10: Pixel A and B Voltages for $x_{quad} = 0.0458$

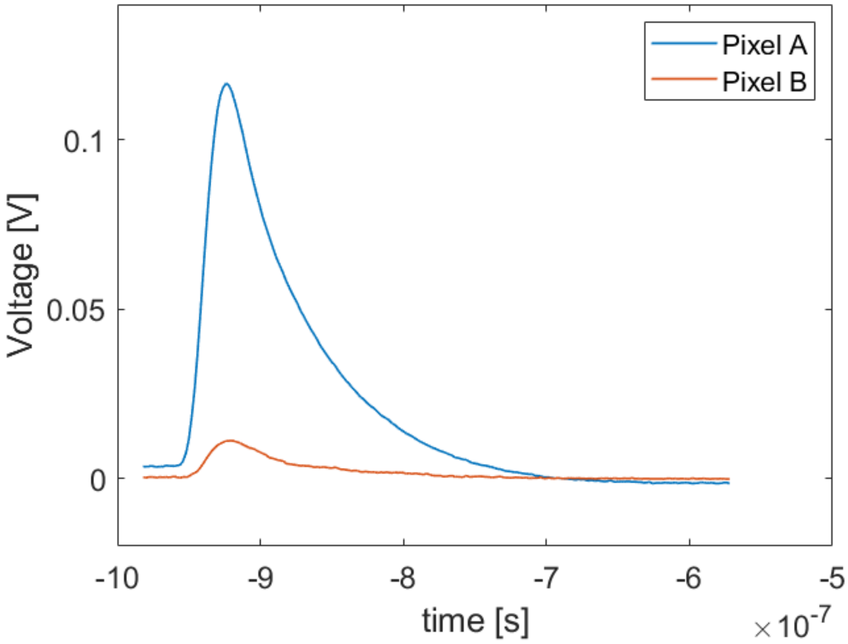

Figure 4-11: Pixel A and B Voltages for $x_{quad} = 0.8353$

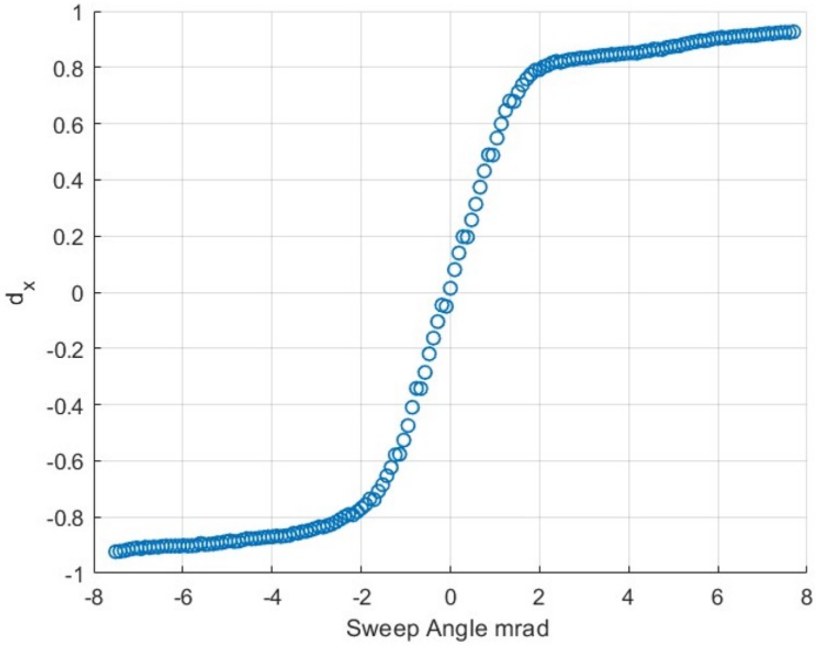

Figure 4-12: Experimental result of quadcell as a beam scans through the x axis.

Figure 4-12 is the consolidation of the SiPM's x_{quad} position at each sweep location. The results of the relative location reported by the SiPM in a quadrant configuration match the behavior of a quadcell detector, transitioning from -1 to 1, with a linear region present where the beam shifts from one pixel to another.

The angular resolution for this experiment is limited by the step size of the steering mirror. Experimentally, the smallest step size of the mirror is measured by calculating the centroid of the beam captured by the camera. The smallest step size corresponds to an angular disturbance of 60 µrad.

The performance of the quadcell detector could not be tested at smaller angle increments due to a limit in the FSM's angular resolution. While the minimum angular resolution of the SiPM could not be evaluated experimentally, the test validates the application of the SiPM as a quadcell detector in low power environments and at high repetition rates.

4.1.3 SiPM High Speed Pulsing Simulation Results

The maximum laser pulse frequency detectable by the C-Series SiPM is modeled with the analysis introduced in Section 3.3. The validity of this approach is verified by comparing the condensed circuit architecture to the traditional multi-source model. The electrical components of the circuit are based off of OnSemi's C-Series SiPM.

A traditional SiPM model with four cells, 3 active, 1 passive, is shown in Figure 4-13. The behavior of a firing cell is simulated as a voltage step response, which produces an avalanche current measured across the shunt resistor. The magnitude of the avalanche current is proportional to the magnitude of the overvoltage and diode capacitance.

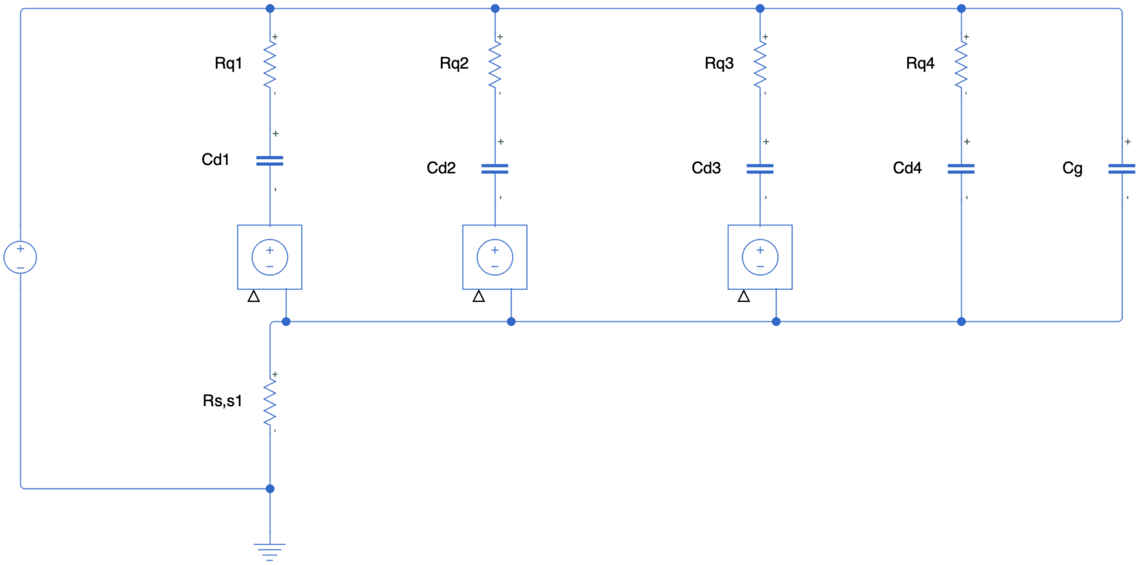

Figure 4-13: Simulink Model of SiPM with 4 microcells and grid capacitance.

The same SiPM with 3 active cells and 1 passive cell is modeled by combining all parallel impedances. Figure 4-14 introduces the simplified circuit. The avalanche current is scaled linearly with the number of cells fired. This is achieved by manipulating the step input voltage. No additional circuit complexity is added to simulate a larger number of cells firing.

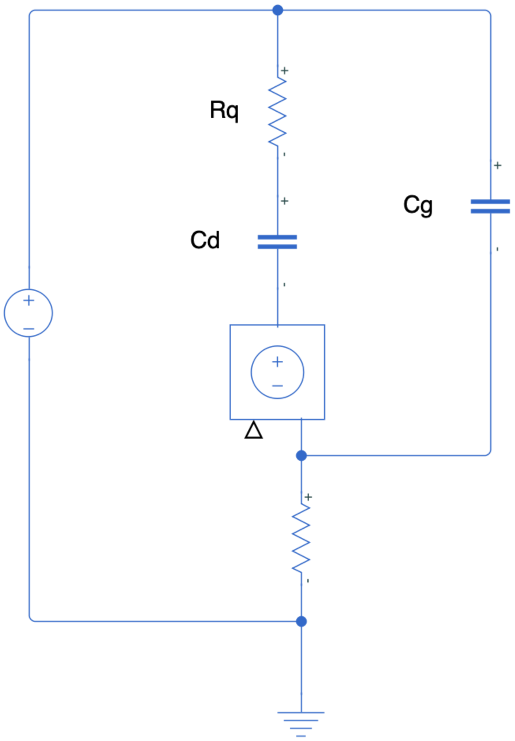

Figure 4-14: Simulink Model of condensed SiPM architecture.

Table 4.2: C-Series SiPM Sensor Parameters [23].

Parameter	Multi-Source	Condensed	Units
R_q	413280	820	Ohms
C_d	1.98×10^{-6}	100×10^{-12}	Farads
C_p	1×10^{-9}	1×10^{-9}	Farads
V_e	5	5	Volts

The circuit parameters used for the simulation are summarized in Table 4.2. Both multi-source and condensed circuit simulations are run with a frequency of 1 kHz and a time step size of 1 ns. The simulation results are shown in Figure 4-16 .

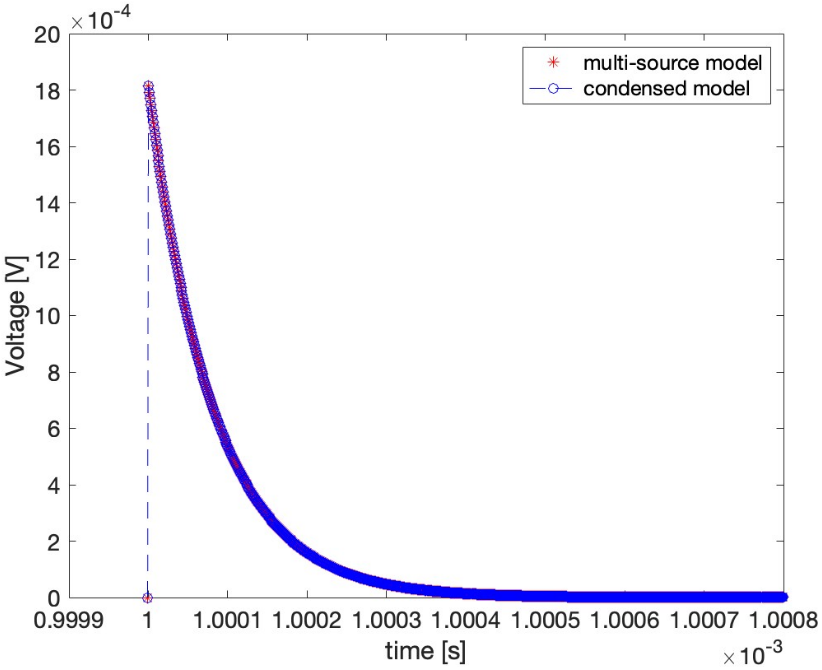

Figure 4-15: Model of SiPM with multiple sources vs. condensed circuit approach.

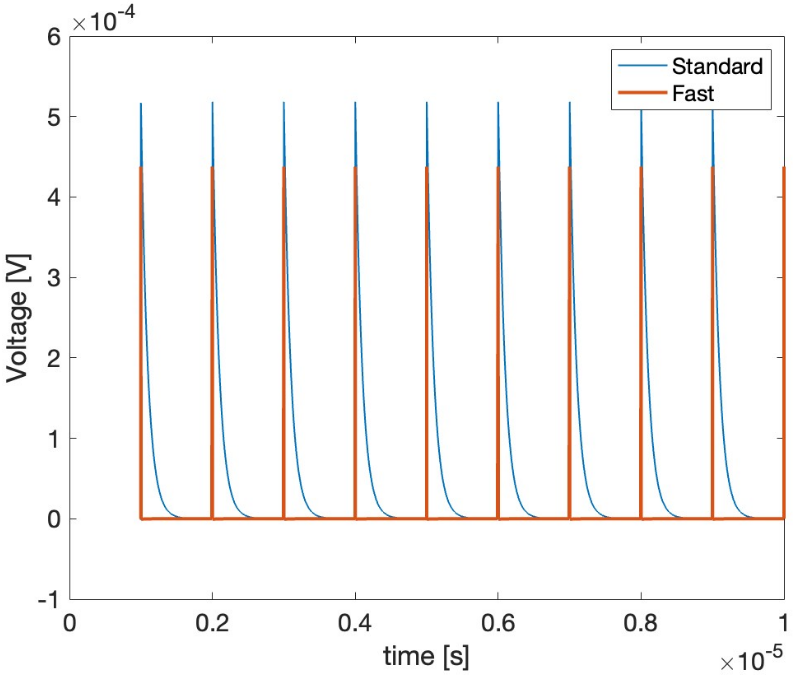

Figure 4-16: Fast and standard output response at 1 MHz repetition rate.

Both simulation outputs are identical, validating the approach presented in this thesis. The simulation results presented in Figure 4-16 showcase the behavior of the standard output compared to the fast output of the SiPM. The detectable pulse rate frequency is limited by the signal pulse width, which is dependent on the R_q and C_d of the circuit model.

When the simulation is run at faster repetition rates, the standard output will begin to "add" itself to the previous pulse since the standard output did not have enough time to reset to equilibrium. If the pulsing frequency is faster than the output's settling time there is a visible DC offset in the standard output. The fast output is also affected by this, but at much higher repetition rates.

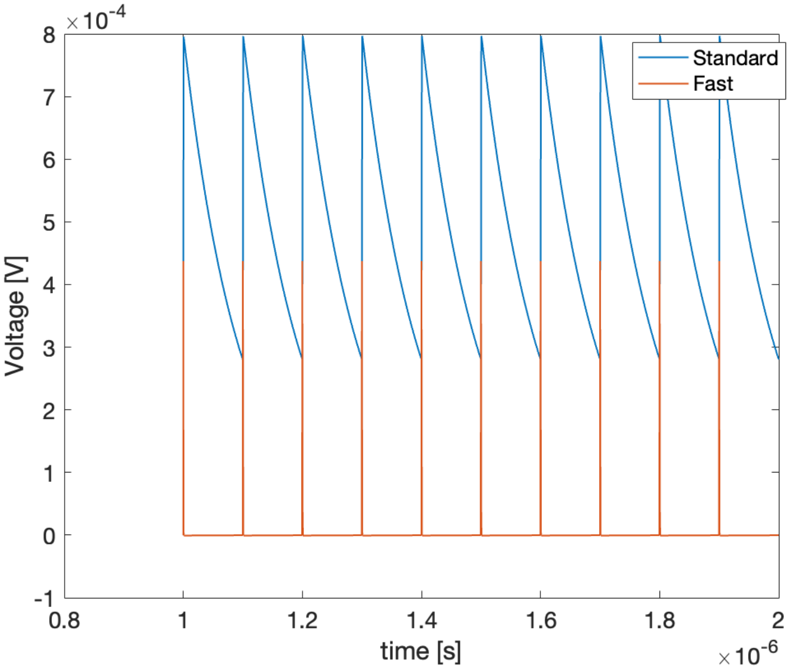

Figure 4-17: Fast and standard output resesponse at 10 MHz repetition rate.

Figure 4-17 shows the DC offset around 0.3 mV when the SiPM is pulsed at a rate of 10 MHz. A simulation of the fast output of the SiPM at varying repetition rates is presented in Figure 4-18. Each pulse models firing of the SiPM micro-cells. Even at a repetition rate of 80 MHz, the pulses are distinguishable from each other.

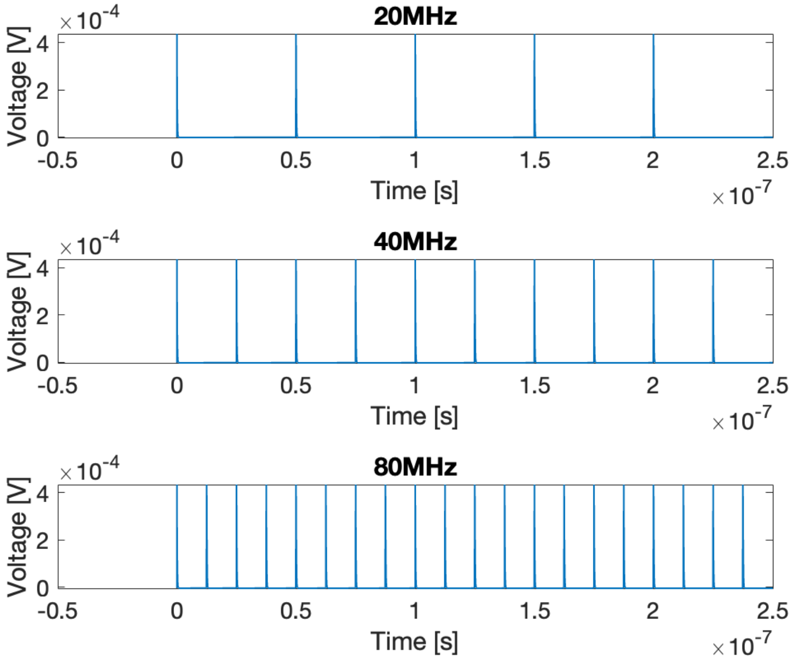

Figure 4-18: Fast output of SiPM at 20 MHz, 40 MHz, and 80 MHz laser pulsing frequencies

The repetition rate is increased until a DC offset begins to appear in the fast output response.

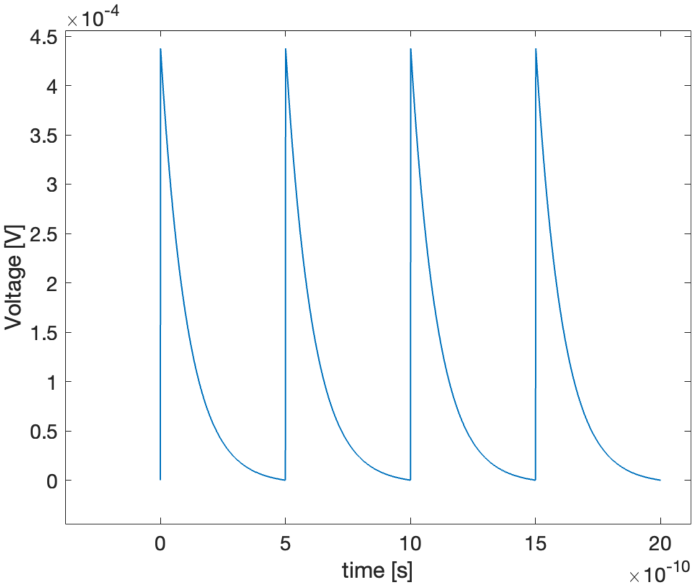

Figure 4-19: Fast Output at 2 GHz with an overvoltage of 5 V.

This corresponds to repetition periods shorter than the sensor's fast output settling time. Figure 4-19 shows that the repetition rate limit is around 2 GHz. This is within the same order of magnitude to the repetition rate established by the signal pulse width of 0.6 ns stated in the data sheet.

Once the behavior of the SiPM simulation is validated with respect to traditional models and the fastest repetition rate is characterized, noise sources are introduced into the simulation. The noise modeling focuses on the incident signal, and as mentioned in Section 3.3, the system is shot noise limited. Shot noise is modeled using a Poisson distribution based on an average expected number of photons. The model introduces noise in the system by varying the voltage amplitude each pulse. Each pulse's amplitude is generated from a Poisson distribution. Figure 4-20 shows the pulse amplitude change each pulse. The number of average photons is 100, so its variance is expected to be $\sqrt{N_{photons}}$.

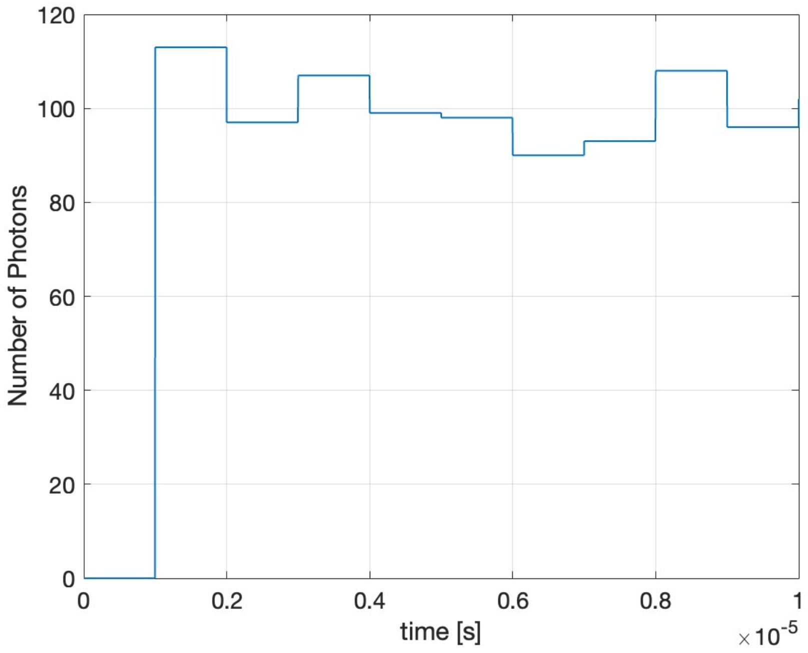

Figure 4-20: Pulses with Poisson Noise at 1 MHz repetition rate.

Both the slow and fast axis are affected by noise. The simulation that yields the results in Figure 4-18 is repeated, but this time introducing shot noise to the system for an expected number of 100 photons per laser pulse.

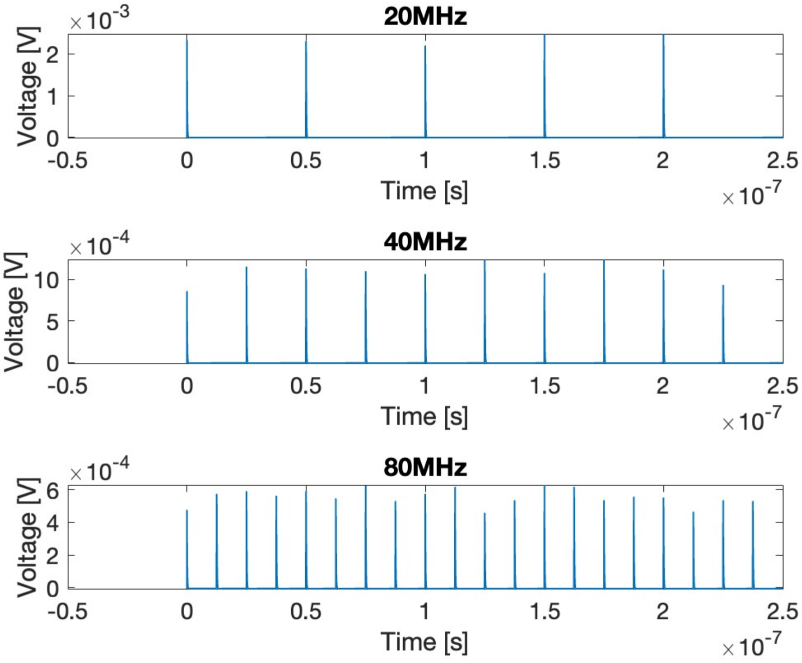

Figure 4-21: High-speed pulsing at different repetition rates, $N_{photons} = 100$.

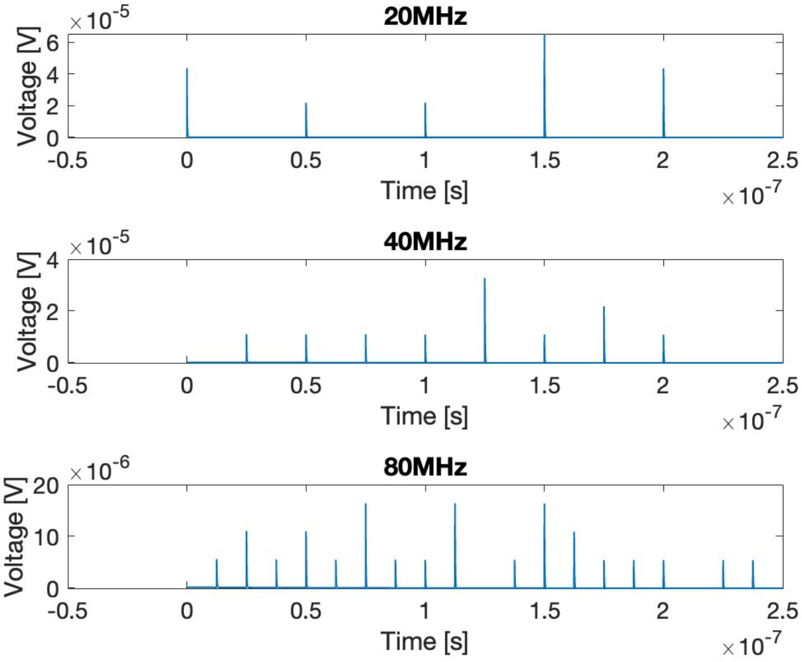

Figure 4-22: High-speed pulsing at different repetition rates, $N_{photons} = 1$.

The simulation is helpful to predict misfiring of cells. Figure 4-22 shows that for a Poisson distribution with an expected number of photons equal to 1 there are cycles where no avalanche current is detected.

The novel methodology of modeling the SiPM microcells as a condensed architecture is helpful in more quickly predicting SiPM behavior at different pulse rates based on the detector geometry, circuit characteristics, and noise distribution of the incident signal. Additionally, the simulation shows that the C-Series SiPM can reliably measure pulses at high speed repetition rates in a low power environment while also providing insight into the response of the detector for single photon pulses. This simulation predicts that for an average number of 100 incident photons, the SiPM is capable of detecting pulses up to 2 GHz.

4.1.4 SiPM High Speed Pulsing Experiment Results

The purpose of this experiment is to validate the simulation described in the previous section by pulsing the C-Series SiPM at repetition rates of 20 MHz, 40 MHz, and 80 MHz. Assuming an OOK communication scheme, the repetition rate of the pulsed laser corresponds to the communication data rate. For example, successfully detecting pulses at 80 MHz corresponds to a data link with 80 Mbps.

In this test, a picosecond pulsed laser is driven at different pulse frequencies. The incident light on the SiPM triggers a current avalanche that is amplified and then measured by an oscilloscope. The results are shown in Figure 4-23, where the fast output of the COTS SiPM is sampled while a laser beam is pulsed at different repetition rates.

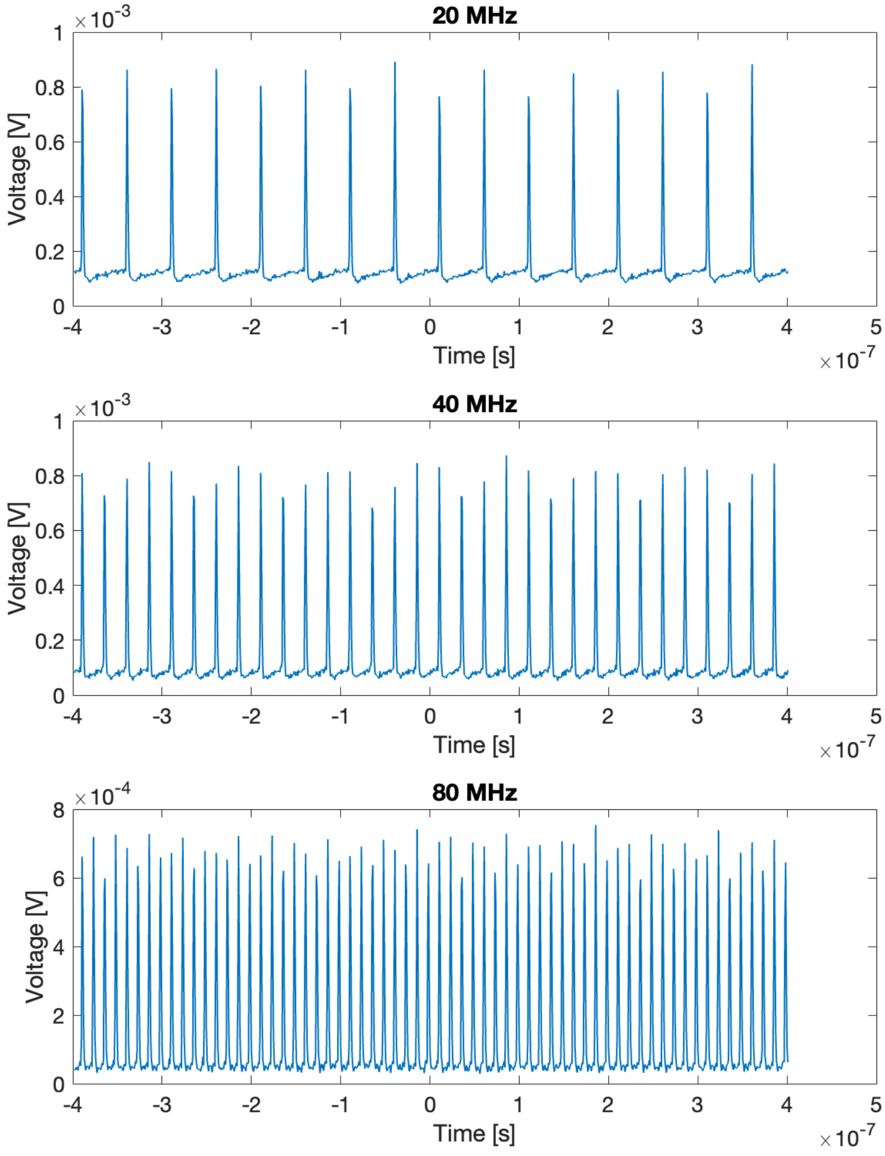

Figure 4-23: High-Speed Pulsing at Different Repetition Rates

The overall output voltage varies slightly at different repetition rates. Since the pulses detected are above the noise floor, each pulse is clearly distinguishable from the noise in the signal and readout circuitry. No missed pulses were measured experimentally for this power level. As the repetition rate increases from 20 MHz to 80 MHz, the time between pulses decreases. Since each pulse has enough time to settle before the next avalanche is triggering, there is no DC offset in the output signal other than the readout noise.

The experimental results confirm that the SiPM is capable of detecting low power pulses at repetition rates of 80 MHz with a clear distinction between the signal's maximum magnitude and the noise floor.

4.2 Summary of Progress

Current free-space optical communication Tx and Rx terminals reach co-alignment by following a beacon-based or beaconless PAT procedure. For the beaconless PAT procedure, the UC after open-loop pointing is reduced by scanning the Tx beam in a spiral sequence [6]. As the Rx terminal detects the Tx beam, the body pointing is corrected, reducing the UC. In beacon-based systems, a different Tx beam with a wider beam divergence is used to measure misalignment between the RX and Tx terminals. In this scenario one detector is used for pointing, and the other for communications.

The results presented throughout Chapter 4 motivate the application of a novel technology that uses the same sensor, a SiPM, to detect misalignment with respect to the transmit beam while receiving data. Similarly to the CLICK-B/C architecture, a MEMS FSM is used to steer the beam during the fine PAT sequence. In this scenario, only a Tx beam and Rx detector are required to establish a crosslink communications in LEO.

The main takeaway of this technology is that the SiPM's ability to report spacecraft body pointing and crosslink data simultaneously reduces the complexity of the optical circuit. The overall SWaP of the terminals is decreased, freeing up volume and resources for additional science equipment of interest.

Additionally, ensemble averaging greatly improves the performance of pointing. The SNR can be increased by either sampling for communication data at a higher rate, or decreasing the pointing update rate. The NEA decreases proportionally with SNR.

Chapter 5

Summary and Future Work

This chapter presents a summary of the simulation and experimental results of the SiPM's performance as a pointing and communication sensor. A SiPM-based lasercom system is compared to the CLICK-B/C terminals, focusing on the SWaP of the PAT and communication subsystems.

The next research steps are then discussed, including improvements to the current experimental setup, modification of the SiPM geometry, custom build of a PCB board for testing, and improved PDE for IR wavelengths.

5.1 Summary

5.1.1 Experiment and Simulation Results

The performance evaluation of OnSemi's SiPMs as a dual use sensor for pointing and communication purposes shows promising results. First, through simulation, the NEA of a SiPM in a quadcell configuration with a 200 µrad and a 1 mm beam diameter is calculated to be close to 1 µrad. The NEA model provides the flexibility to test the performance of the SiPM with different parameters, such as the pixel size, beam diameter, and pixel gap length.

When calculating the NEA for different beam diameters, it is clear that smaller size beams result in higher angular sensitivity at the cost of a decreased dynamic range. However, the size of the beam is constrained by the gap length between pixels. If the gap length is greater than the beam diameter, then the quadcell loses information and is incapable of providing a relative position estimate.

Table 5.1: Simulation NEA for various beam diameters.

Diameter [mm]	NEA [µrad]
.2	0.88
1	1.33
2	2.69
4	5.59
6	9.14
10	25.77

The experiment carried out simulates the power environment desired by attenuating the laser light with an OD filter. Each laser pulse incident on the SiPM is calculated to contain approximately 100 photons. An angular disturbance is introduced by a fast steering mirror. This angular disturbance is then converted into a linear offset by placing a 50 mm focal length lens right before the SiPM. The lens works as a transform agent that converts an angular disturbance into a linear displacement. A change in angle generated by the FSM is measured by the quadcell SiPM. The angular resolution reported by the SiPM is limited by the minimum step size of the FSM. This step size is calculated to be equivalent to 60 µrad. Even though it was not possible to experimentally test angular resolution in the order of 1 µrad, the test shows that a SiPM quadcell can report a relative offset at a repetition rate of 1 MHz.

The performance of the SiPM as a communication sensor is tested by evaluating the fastest repetition rate detectable both through simulations and experiments. A novel method that simulates SiPM arrays with N number of cells is introduced. The first key advantage of the model is that the avalanche current from a firing cell is modeled as a scaled step response rather than an impulse response. This corresponds to a simulation that is not limited by the resolution of an impulse signal generated by software. Simulations can simulate a step response more accurately than an impulse response. The second advantage is the condensed architecture analysis. An N microcell pixel is modeled as a circuit with combined impedances that match the traditional architecture and a source that is scaled by the number of firing cells. A C-Series SiPM with 504 micro-cells is modeled and tested at different repetition rates. The calculated theoretical limit from the fast axis is around 2 GHz.

Experimentally, the SiPM is tested at 20 MHz, 40 MHz, and 80 MHz. The SiPM's fast output signal is capable of detecting all three test repetition rates, as showin in Figure 4-13. The repetition rate was not pushed further due to pulsing limitations in the laser driver.

Both simulation and experimental results of the angular resolution and high pulse rate detection in low power environments demonstrate the SiPMs applicability as a lasercom systems in LEO.

5.2 Discussion/Comparison of SWAP based system vs APD system (CLICK-B/C)

This subsection explores the benefits and possible drawbacks of using a SiPM as a dual communication and pointing sensor for crosslinks in LEO. The CLICK-B/C mission is used as a reference to evaluate performance metrics such as SWaP, data rates, and pointing accuracy.

The 1.5U CLICK-B/C terminals transmit 1550 nm light at an average power of 200 mW for communication, and 980 nm light at 250 mW for beacon pointing. The communication link can go up to 20 Mbps for link distances ranging from 25 km to 580 km.

The experimental results in this thesis show that a 450 nm laser transmitting light with an average power of 17.6 mW triggers avalanche currents in a SiPM at rates up to and higher than 80 Mbps, assuming OOK. This data rate is achievabble at crosslink ranges up to 1000 km.

Figure 2-12 shows the top view of CLICK B/C's optical bench. The optical paths for the beacon (green), Tx (red), and Rx (blue) highlight the volume used for fine PAT and data communication. This volume, as measured in CAD, is equal to $58.5\,\text{cm}^3$.

In Figure 2-13, a 2x2 SiPM array with a total area of $36\,\text{mm}^2$ is placed on the optical bench instead of the APD and quadcell. This proposed configuration reduces the volume occupied by the fine PAT and data communication system. The measured volume is decreased to $20.4\,\text{cm}^3$. A volume reduction of 65% gives room for additional science or spacecraft bus equipment to be integrated into the smallsat.

Table 5.2: Performance Comparison

	CLICK-B/C	SiPM	Units
Volume	58.5	20.4	cm^2
P_{Tx}	450	17.6	mW
V_{bias}	60	30	V
NEA	1.83	1.33	μrad
Data Rate	20	100	Mbps

Removing the APD and Quadcell reduces the bias voltage required to operate the components and the volume used for PAT. The operating voltage for the APD is 60 V. In contrast, the operating bias of the SiPM is 30 V. Table 5.2 summarizes the SWaP comparison between CLICK-B/C and the SiPM configuration. For all of the categories shown, the SiPM configuration has higher performance for lower power requirements. It is important to note that the NEA of the SiPM can be reduced further by taking advantage of ensemble averaging, which is dependent on the difference between the data update rate and the the pointing update rate.

5.3 Future Work

With experimental and simulation results which confirm that a SiPM can be used as a communications and pointing sensor in low power environments, it is of interest to further improve the technology by modifying the current test setup and simulations, adjusting evaluation board design for reduced gap length between pixels, and researching the possibility of doping the silicon junction for higher PDE at wavelengths closer to IR.

5.3.1 Improvements to current Test Setup and Simulation

The first steps to further evaluate the NEA of the SiPM as a quadcell is to increase the resolution of the angular disturbance. An FSM with a step size smaller than 1 µrad is required in order to test the theoretical NEA of OnSemi's SiPM. Similarly, a high speed pulsing laser with a repetition rate greater than 2 GHz and measuring equipment with adequate bandwidth are needed to test the theoretical simulation limit.

Developing a predictive model that outputs an expected data rate based on a Tx power would be a helpful tool for visualizing the performance of the SiPM as a communication sensor in different power environments. This model differs from the condensed approach introduced in this thesis since it no longer assumes all incident photons arrive at exactly the same time. A Monte Carlo simulation can be used to model firing cells not detecting incident photons due to incomplete quenching for data rates faster than the signal pulse width. The Monte Carlo simulation essentially calculates the probability of this event happening for various Tx power levels. This simulation integrates the effects of dark count noise and readout noise in order to estimate the noise equivalent power (NEP) of the detector.

5.3.2 Pixel Gap Length Design for SiPM Quadcell Array

The performance of the SiPM for pointing can be improved by adjusting the gap size between pixels relative to the beam diameter. For a beam diameter of 0.2 mm the NEA would be maximized with a pixel gap in the same order of magnitude. The physical testing of the SiPM would be more reilable if a custom PCB board was designed. Currently, OnSemi's array evaluation boards rely on jumper wires for testing the fast and standard outputs. These wire connections are susceptible to noise and not reliable for high frequency signals at low voltage levels. The goal is to design and build a PCB board with the desired SiPM pixel geometry that provides access to the fast and standard outputs of each pixel in the array through low noise SMA connections. This will allow for easy interface to the board for simultaneous pointing and communication demonstrations.

5.3.3 SiPM doping for PDE improvement at IR wavelengths

This technology is aimed to be used for crosslinks in LEO. In this environment, photodetectors will encounter sources of noise such as sunlight. The power spectral density of the sun can be approximated to resemble the radiation given off by a black body, shown in Figure 5-1. The power spectral density is highest for the 400 nm to 600 nm wavelength range. For the C-Series SiPM, the photon detection efficiency is highest at 450 nm.

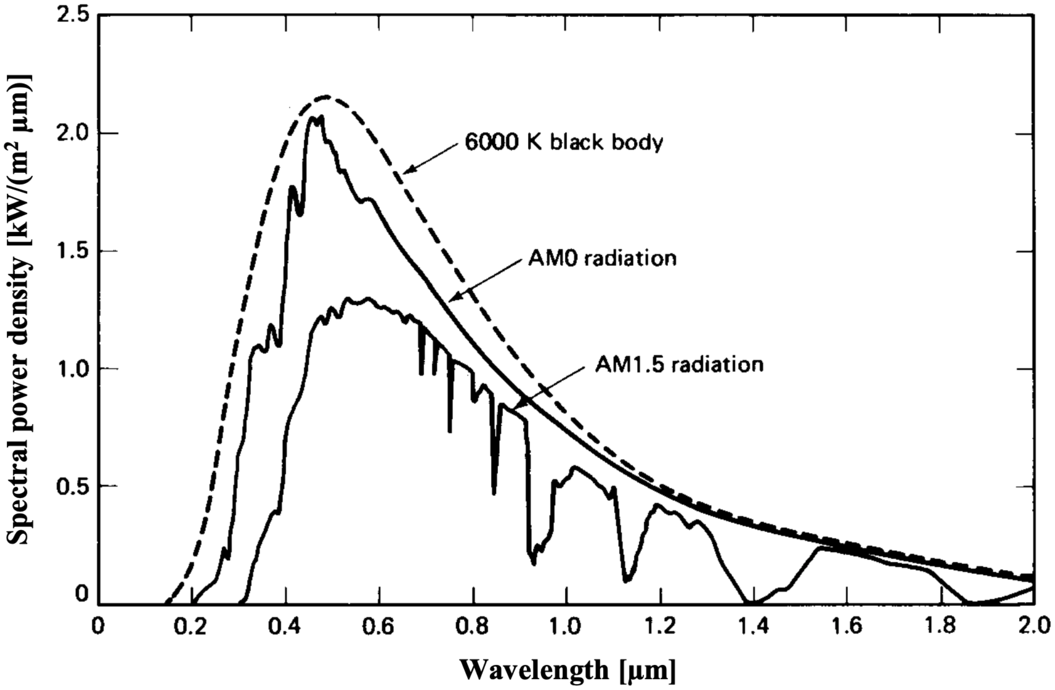

Figure 5-1: Spectral Power Density of the Sun [29].

The solar spectrum matches the PDE curve for the detector, introducing noise in the communication signal if not addressed by filtering or modulation. This can be avoided by modulating the transmit light and introducing a filter in the receive terminal to only pass the modulation frequency of the communication signal. The effect of the sun on the sensor can also be reduced by doping the semiconductor junction of the SiPM such that the PDE is maximum at higher wavelengths. Companies such as Hamamatsu and SensL are currently developing p-n junction SiPMs with increased PDE in the 1 µm range, such as the S13270 and R-Series detectors [30]. For detection closer to the near infrared, devices constructed from InGaAs allow low light detection in the 900 nm - 1700 nm range.

By modifying the doping of the semiconductor specifically to increase its PDE at NIR wavelengths, the power level of the signal can remain low without having to compensate for solar radiation. This future work effort would evaluate the feasibility and challenges of manufacturing a SiPM detector with different Silicon doping properties.

5.3.4 Live Hardware Demonstration

To bring together the efforts mentioned in this section, we aim to design a test module that is representative in SWaP of a SiPM based lasercom terminal which demonstrates simultaneous pointing and communication capabilities. This experimental setup will integrate a secondary FSM used to correct the angular disturbance introduced by the primary FSM with a frequency up to 1 kHz. At the same time, the SiPM must report an encoded bit stream sent by a pulsed laser. The successfully demonstration of this procedure in a vacuum and low power environment will showcase the readiness of this technology for LEO lasercom applications.

Bibliography

[1] Federal Communications Comission. History of commercial radio, 2023. URL `https://www.fcc.gov/media/radio/history-of-commercial-radio#:~:text=November%202%2C%201920,Harding%20and%20James%20Cox`. Last accessed 15 April 2024.

[2] Bryce Tech. Smallsats by the numbers, 2023. URL `https://brycetech.com/reports/report-documents/Bryce_Smallsats_2023.pdf`. updated july 2023.

[3] Prof. D. J. Blumenthal. Lecture notes in photodetectors, Spring 2011.

[4] OnSemi. Introduction to the silicon photomultiplier (sipm), 2023. URL `https://www.onsemi.com/pub/Collateral/AND9770-D.PDF`. Last accessed 15 April 2024.

[5] Sergei Dolinsk, Geng Fu, and Adrian Ivan. Timing resolution performance comparison for fast and standard outputs of sensl sipm. pages 1–6, 2013.

[6] CCSDS. Ccsds orange book optical high data rate (hdr) communication. *CCSDS 141.11-O-1*, Washington DC: CCSDS, 2018.

[7] Peter Grenfell, Paul Serra, Ondrej Cierny, William Kammerer, Grant Gunnison, Joseph Kusters, Cadence Payne, and Kerri Cahoy. Design and prototyping of a nanosatellite laser communications terminal for the cubesat laser infrared crosslink (click) b/c mission. 2020.

[8] Gianluca Giustolisi, Paolo Finocchiaro, Alfio Pappalardo, and Gaetano Palumbo. Behavioral model of silicon photo-multipliers suitable for transistor-level circuit simulation. *Electronics*, 10:1551, 2021.

[9] OnSemi. Silicon photomultiplier (sipm) high fill-factor arrays, 2023. URL `https://www.onsemi.com/pdf/datasheet/arrayj-series-d.pdf`. Last accessed 16 December 2023.

[10] OnSemi. J-series sipm sensors, 2023. URL `https://www.onsemi.com/pdf/datasheet/microj-series-d.pdf`. Last accessed 16 December 2023.

[11] Tektronix. Mixed domain oscilloscope. URL `https://www.tek.com/en/datasheet/mixed-domain-oscilloscopes-0`. Last accessed 1 May 2024.

[12] Thorlabs. Npl series nanosecond pulsed lasers user guide, 2023. URL `https://www.thorlabs.com/drawings/c482c5a07533568-19C76195-F5E7-6C5E-7DA2C6D0C93BD188/NPL45B-Manual.pdf`. Last accessed 15 April 2024.

[13] Thorlabs. Large beam diameter scanning galvo systems. URL `https://www.thorlabs.com/drawings/42c8b4ebb3873fee-143C6DD9-C771-DC97-B116CC4DAF3954FC/GVS012-Manual.pdf`. Last accessed 12 April 2024.

[14] iDS Imaging. Ui-5490se-c-hq, 2024. URL `https://www.ids-imaging.us/download-details/AB.0010.1.41902.24.html`. Last accessed 30 April 2024.

[15] Louis J. Ippolito. *Satellite Communication systems Engineering: Atmospheric Effects, Satellite Link Design and System Performance.* John Wiley Sons Ltd, 2017.

[16] Hui Rongquing. *Introduction to Fiber-Optic Communications.* Academic Press, 2020.

[17] Andrea Goldsmith. *Wireless Communications.* Cambridge University Press, 2005.

[18] D.J Griffiths. *Introduction to Quantum Mechanics.* Prentice Hall, Upper Saddle River NJ, 1995.

[19] MKS Newport. Laser beam spatial profiles. URL `https://www.newport.com/n/laser-beam-characterization#:~:text=is%20also%20given.-,Gaussian%20Beams,concentrated%20close%20to%20the%20axis`. Last accessed 15 April 2024.

[20] Nikolai Pavlov, Gunnar Mæhlum, and Dirk Meier. Gamma spectroscopy using a silicon photomultiplier and a scintillator. 2006.

[21] F. Corsi, C. Marzocca, A. Perrotta, A. Dragone, M. Foresta, A. Del Guerra, S. Marcatili, G. Llosa, G. Collazzuol, G. F. Dalla Betta, N. Dinu, C. Piemonte, G. U. Pignatel, and G. Levi. Electrical characterization of silicon photo-multiplier detectors for optimal front-end design. 2006.

[22] Stefan Seifert, Herman T. van Dam, Jan Huizenga, Ruud Vinke, Peter Dendooven, Herbert Löhner, and Dennis R. Schaart. Simulation of silicon photomultiplier signals. *IEEE Transactions on Nuclear Science*, 56(6):3726–3733, 2009.

[23] OnSemi. Silicon photomultiplier (sipm) high fill-factor arrays, 2023. URL `https://www.onsemi.com/pdf/datasheet/microc-series-d.pdf`. Last accessed 16 December 2023.

[24] Mini-Circuits. Low noise amplifier, 2023. URL `https://www.minicircuits.com/pdfs/ZFL-1000LN+.pdf`. Last accessed 16 December 2023.

[25] PicoQuant. Picosecond pulsed drivers, 2023. URL `https://www.picoquant.com/products/category/picosecond-pulsed-driver/pdl-828-sepia-ii-computer-controlled-multichannel-picosecond-diode-laser-driver#description`. Last accessed 16 December 2023.

[26] Masahiro Toyoda, Kenichi Araki, and Yoshiaki Suzuki. Measurement of the characteristics of a quadrant avalanche photodiode and its application to laser tracking system. *SPIE Optical Engineering*, 41(1):254–256, January 2002. doi: https://doi.org/10.1117/1.1418222.

[27] Gabriele Adamo, Antonino Parisi, Salvatore Stivala, Alessandro Tomasino, Diego Agrò, Luciano Curcio, Giuseppe Costantino Giaconia, Alessandro Busacca, and Giorgio Fallica. Signal to noise ratio of silicon photomultipliers measured in the continuous wave regime. 2014.

[28] Tom Thomas. Ensemble averaging filter for noise reduction. 2016.

[29] Prof. Miro Zeman. Solar radiation, 2023. URL `https://ocw.tudelft.nl/wp-content/uploads/Solar-Cells-R2-CH2_Solar_radiation.pdf`. Last accessed 18 April 2024.

[30] Paul Horowits and Winfield Hill. *The Art of Electronics.* Cambridge University Press, 2020.